



Three-dimensional numerical investigation on flow past two side-by-side curved cylinders

Yangyang Gao^{a,*}, Jianyong He^a, Muk Chen Ong^b, Ming Zhao^c, Lizhong Wang^a

^a Ocean College, Zhejiang University, Zhoushan, 316021, PR China

^b Department of Mechanical and Structural Engineering and Materials Science, University of Stavanger, 4036, Stavanger, Norway

^c School of Engineering, Design and Built Environment, Western Sydney University, Penrith, 2751, NSW, Australia

ARTICLE INFO

Keywords:

Convex curved cylinder
Spacing ratio
Vorticity structures feature
Axial flow
Mean pressure coefficients

ABSTRACT

Three-dimensional numerical simulations of flow past two side-by-side convex curved cylinders are performed for various spacing ratios ($1.25 \leq L/D \leq 5$) and Reynolds numbers ($100 \leq Re \leq 500$). A comprehensive investigation of the effects of spacing ratio and Reynolds number on the wake flow features, pressure coefficients and axial flow velocity is conducted. Four flow patterns: a single bluff body pattern, biased flow pattern, coupling vortex shedding pattern and co-shedding pattern are identified for the vertical straight sections. The flows along the curved sections of two cylinders are classified into five flow regimes: normal shedding, vortex dislocation, oblique shedding, non-shedding and instability of shear layer regimes. It is revealed that at $L/D = 1.5$, the switchover of the gap flow deflection along the curved spans leads to the oblique vortex shedding pattern for $Re = 100$ and 300. The Reynolds stress intensity, vortex strength, and the mean pressure coefficient are found to be reduced significantly from the vertical to the horizontal sections of the cylinders. With the increase of the spacing ratio, the axial flow velocity increases along the curved span of two cylinder, whereas the absolute value of base coefficient decreases.

1. Introduction

The complex flow in the wake of multiple cylinders in side-by-side configuration has attracted considerable attention due to its relevance to offshore and ocean engineering applications, such as risers, pipelines and cables etc. The top ends of the catenary risers and mooring lines are attached on the floating production system and the horizontal parts near the bottom ends are laid on the seabed, resulting in curved spans between the touch down points and the vertical pipes. The changing local inclination angle along the span of the curved cylinders contributes to a wake flow much more complex than the ones behind straight cylinders.

Numerous numerical studies on flow past a single curved cylinder have been performed to investigate the effects of the Reynolds number, the curvature radius and flow direction on the flow behaviors, Strouhal numbers and force coefficients (Miliou et al., 2003, 2007; Canabes, 2010; Gallardo et al., 2013, 2014; Assi et al., 2014; Shang et al., 2018; Jiang et al., 2018, 2019; Jiang et al., 2018a,b, 2019; Zhu et al., 2018, 2019). It was found that at low Reynolds numbers, the curvature of cylinder induces the out-of-phase mode of the vortex tubes along the curved span of the single cylinder (Miliou et al., 2007; Gallardo et al.,

2014a,b), the vortex tubes are deformed and the phase of vortex shedding is shifted close to the horizontal section. However, the vortex tubes are almost parallel to the cylindrical axis and vortex shedding is in-phase mode along the span at high Reynolds numbers. The wake flow features of flow past a curved cylinder with convex and concave configurations are very different from each other (Miliou et al., 2003, 2007), the vortex tubes are slightly inclined and follow the curved span. Only a single predominant vortex shedding frequency exists along the span in the convex case, while the vortex shedding is significantly suppressed by the axial flow in the concave case. Gallardo et al. (2014a,b) and Canabes (2010) performed a series of numerical simulation to investigate the three-dimensional flow instabilities for a convex curved cylinder. The spanwise velocity changes drastically due to the effect of curvature, resulting in larger mean pressure gradient in the upper part of the cylinder where the cylinder axis is perpendicular to the flow. Gallardo et al. (2014a,b) further investigated the turbulent wake behind the convex curved cylinder with horizontal and vertical extensions at subcritical Reynolds number $Re = 3900$. The results show that the vorticity strength is significantly reduced and the three-dimensional characteristics are drastically enhanced near the horizontal section. The turbulent wake

* Corresponding author.

E-mail address: yygao@zju.edu.cn (Y. Gao).

and Reynolds stress intensity for a convex curved cylinder vary along the span of a curved cylinder (Gallardo et al., 2014a,b). The wake flow features such as reverse flow region and roll-up of shear layers gradually disappear near the horizontal extension. Similarly, the Reynolds stress magnitude is reduced along the curved span, which is attributed to combined effects of the weak vortices strength and existence of the axis flow. Gallardo et al. (2013) and Jiang et al. (2018a,b) found the attached extension reduces the effect of the boundary condition on the wake of curved section. Jiang et al. (2018a,b) investigated the flow past a concave curved cylinder at low Reynolds numbers and classified the flow into three different flow regimes: non-shedding, oblique shedding and parallel shedding. Shang et al. (2018) performed a series of experiments on flow past a concave and convex curved cylinders at different Reynolds numbers and aspect ratios. The spanwise velocity and streamwise vorticity are found to increase with the increase of the curvature at concave configuration and the vortex shedding is completely suppressed when the curvature is sufficiently high.

When multiple cylinders are arranged in a side-by-side configuration, the wake flow features become more complex and are affected by the spacing ratio L/D (where L is the center-to-center spacing between two cylinders and D is the cylinder diameter) and the Reynolds number Re (where $Re = UD/v$, U is the free-stream velocity and v is the kinematic viscosity of the fluid) (Sumner et al., 1999, 2010; Xu et al., 2013; Alam et al., 2003, 2007, 2011, 2013; Tong et al., 2014, 2015). Depending on L/D and Re , the wake flow pattern could present as a single street, asymmetrical flow and two coupled streets. Alam and Zhou, 2013 observed four flow regimes with the increase of L/D for two side-by-side square cylinders, i.e. the single bluff body regime, the asymmetric regime, the transition regime and the coupled vortex street regime. At an intermediate spacing ratio, the gap flow is deflected towards one cylinder, resulting into a narrow wake and a wide wake behind the two cylinders, respectively. The deflection direction of the gap flow switches from one cylinder to another intermittently, forming a flip-flop flow pattern (Ishigai et al., 1972). Extensive experimental and numerical studies have been performed to investigate the mechanisms of the gap flow deflection for two side-by-side straight cylinders. Afgan et al. (2011) observed narrow and wide wakes for two side-by-side cylinders at subcritical Reynolds numbers, and as the spacing ratio increases, the vortex streets become symmetrical. The narrow and wide wakes are formed due to the anti-phase gap vortices that are close to each other (Alam and Zhou, 2013). Wang and Zhou (2005) reported that the asymmetrical flow regime could be divided into the stably deflected gap flow and changeover of the gap flow deflection regimes. Gao et al., 2020 performed a series of experiments to investigate the effect of the inclination angle on the gap flow patterns behind two and three side-by-side cylinders. The switch-over phenomenon from the deflected flow pattern into the flip-flop pattern is observed when the inclination angle is in a certain range. The spacing ratio is found to have a significant effect on the force coefficient, as L/D increases, the force coefficient and mean pressure coefficients decrease (Bearman and Wadcock, 1973; Vu et al., 2016). The reason for the formation of gap flow and its direction changeover is explained by Wang and Zhou (2005). They found that when the vortices in the wide wake are in phase, and the opposite-signed vortices in the narrow wake are engaged in pairing, the gap flow is deflected to one side due to the formation of a low pressure zone. The phase lagging of the vortices existed between the wide and narrow wakes will lead to the changeover of the gap flow deflection from one side to another.

As mentioned above, most of the previous studies are focused on the flow behaviors behind two side-by-side straight cylinders that are perpendicular to the flow direction. There is a lack of information on the effects of the spacing ratio and the Reynolds number on the wake flow features along the curved spans of two cylinders. Therefore, the principal aim of the present study is to investigate the three-dimensional flow characteristics behind two side-by-side curved cylinders at different spacing ratios and Reynolds numbers. The paper is organized

as follows. The numerical methods and model validation are described in Section 2 and 3. In Section 4, the results for the instantaneous wake flow patterns, time-averaged flow fields, axis flow characteristics and mean pressure coefficients are presented. Finally, the conclusions are drawn in Section 5.

2. Numerical method

Fig. 1 shows a sketch of the computational domain for simulating flow past two parallel side-by-side curved cylinders with the same diameter of D and a center-to-center distance of L . The diameter of each cylinder is 0.01m. Each cylinder comprises a horizontal straight section, a vertical straight section and an arc section with a 90° angle and a radius of $R = 12.5D$. Flow past a same single cylinder has been widely used in the previous numerical studies (Miliou et al., 2003, 2007, 2007; Gallardo et al., 2014a,b; Jiang et al., 2018a,b). The spacing ratio L/D is varied from 1.25 to 5. The parameters L_v and L_h are defined as the vertical straight extension length and horizontal straight extension length, respectively. The lengths of the horizontal and vertical straight extensions are $L_h = 10D$ and $L_v = 6D$, respectively, which are sufficiently long to ensure negligible effects of the top and right boundaries on the flow features of the curved part of the cylinder (Gallardo et al., 2013; Jiang et al., 2018a,b).

The computational domain is 32.5D long in the streamwise direction (x -direction), 20D+L wide in the y -direction and 28.5D high in the z -direction. The inlet boundary is located 10D from the center of vertical portion, the distance between the bottom boundary and the horizontal cylinder is 10D. Two lateral side boundaries are located 10D from the centers of two cylinders. The horizontal section of the cylinder ends at the outlet boundary. The parameter s is defined as the distance from the top end of the curved part along the cylinder span, i.e. $s = R\phi$, where ϕ is the local inclination angle of the curved axis with respect to the vertical direction. The uniform flow is parallel to the planes of two curved cylinders, i.e. the system is in a convex arrangement. For the purpose of convenience, the two side-by-side cylinders are labeled as C1 and C2, respectively.

Direct numerical simulation (DNS) is used to simulate the flow past two side-by-side curved cylinders. The flow past two side-by-side curved cylinders is governed by the three-dimensional incompressible Navier-Stokes equations:

$$\frac{\partial u_i}{\partial t} + u_j \frac{\partial u_i}{\partial x_j} = -\frac{1}{\rho} \frac{\partial p}{\partial x_i} + \nu \frac{\partial^2 u_i}{\partial x_j \partial x_j} \quad (1)$$

$$\frac{\partial u_i}{\partial x_i} = 0 \quad (2)$$

where the coordinates $x_1 = x$, $x_2 = y$ and $x_3 = z$, u_i is the fluid velocity in the x_i -direction, t is the time, ρ is the fluid density, p is the pressure and ν is the kinematic viscosity.

The Navier-Stokes equations are solved using the Open Source Field Operation and Manipulation (OpenFOAM® v1806) C++ libraries. The icoFoam solver is adopted in the present study. The convection terms are discretized using the second-order cell-limited Gauss linear scheme, the pressure terms and Laplace terms are discretized using the second-order Gauss linear scheme. The velocity and pressure coupling fields are solved by PISO (pressure implicit with splitting of operators) algorithm. The second order Crank Nicholson implicit scheme is adopted for the temporal discretization.

A uniform flow velocity is imposed on the inlet boundary, i.e. $u_i = (u, v, w) = (U, 0, 0)$, where u , v and w are the velocities in the x -, y - and z -directions, respectively. Three flow velocities are set to be $U = 0.01$ m/s, 0.03 m/s, 0.05 m/s, corresponding to Reynolds numbers $Re = 100, 300$ and 500, respectively, the viscosity of the fluid is 1×10^{-6} m²/s. No-slip boundary is employed on the surfaces of the two cylinders, the velocity is zero. A symmetry boundary condition is given to the top boundary, i.e.

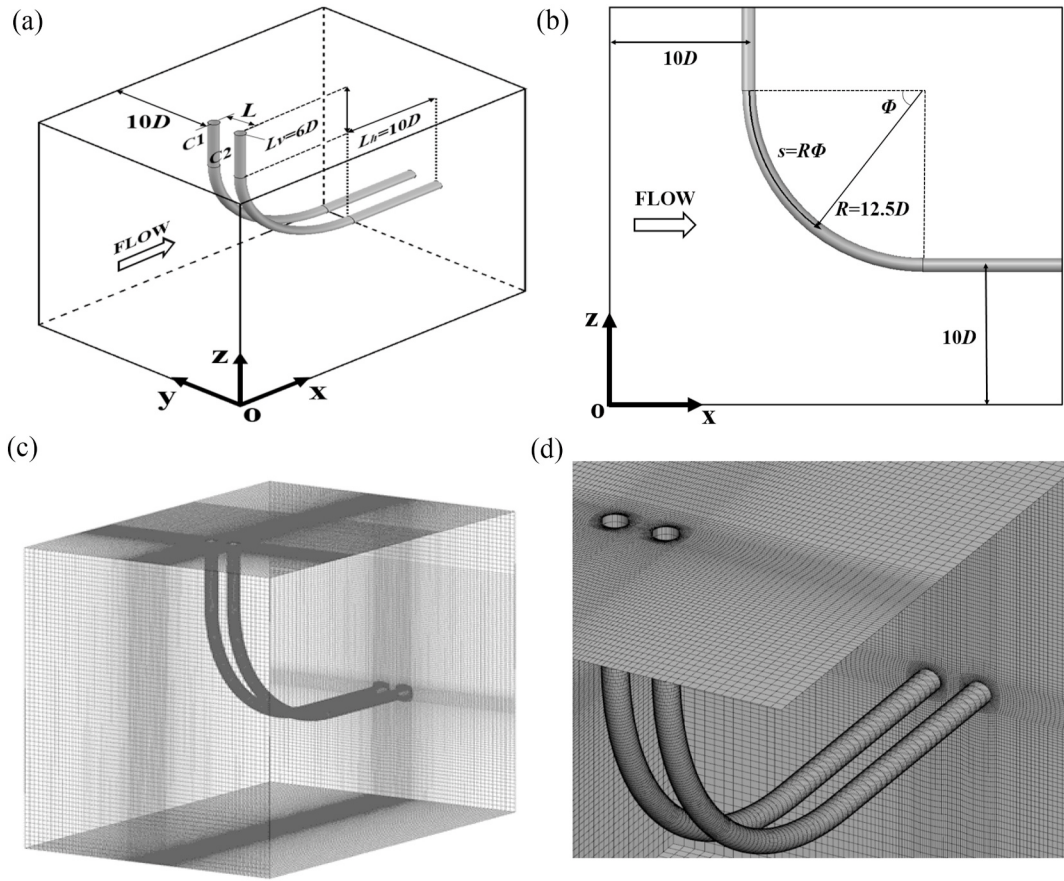


Fig. 1. The schematics of the computational domain and mesh of the two side-by-side curved cylinders: (a) 3-D view of computational domain, (b) front view of the computational domain, (c) three-dimensional view of mesh, (d) the mesh details for two curved cylinders.

$\partial u / \partial z = 0, \partial v / \partial z = 0, w = 0$ and $\partial p / \partial z = 0$. On the outflow boundary, the Neumann boundary condition is applied for velocity, i.e. $\partial u / \partial x = 0, \partial v / \partial x = 0$ and $\partial w / \partial x = 0$, and the pressure is set to zero. Free slip condition is applied on the two lateral boundaries (i.e. $v = 0, \partial u / \partial y = \partial w / \partial y = 0, \partial p / \partial y = 0$) and bottom boundary (i.e. $w = 0, \partial u / \partial z = \partial v / \partial z = \partial p / \partial z = 0$). The non-dimensional computational time step $\Delta t U / D = 0.01$ is adopted to ensure the maximum Courant number of 0.55, which is sufficient to ensure the stability and convergence of the numerical simulations.

3. Mesh dependency study and numerical validation

To test the mesh dependency, flows past a straight cylinder and single curved cylinder at $Re = 100$ and 500 are simulated using three meshes with different densities. The non-dimensional distance between

the first layer mesh node next to the cylinder and the cylinder surface defined as $y^+ = u_f \Delta / \nu$ (where u_f is the friction velocity and Δ is the radial distance between a mesh node and the cylinder surface). The radial size of the cell on the cylinder surface is 0.06 and 0.01 for $Re = 100$ and 500 , respectively. **Table 1** shows the comparison of the numerical results obtained from meshes with different densities, where Δx_{\min} is the minimum mesh size in the streamwise direction. The comparisons of the mean drag coefficient $\overline{C_D}$, root-mean-square lift coefficient C'_L and Strouhal number St obtained from the medium mesh with literature results at $Re = 100$ and 500 are presented in **Table 2**. The drag and lift coefficients C_D and C_L , pressure coefficient C_p and Strouhal numbers St are defined as follows:

$$\overline{C_D} = \frac{2F_D}{\rho A U^2} \quad (3)$$

Table 1

Comparisons of the numerical results of a straight cylinder and a curved cylinder with three meshes at $Re = 100$ and 500 .

Re	Case	Mesh density	$\Delta x_{\min}/D$	Wall unit y^+	Node number	$\overline{C_D}$	C'_L	St
100	Straight cyl	coarse	0.06	0.571	523109	1.378	0.248	0.168
		medium	0.03	0.457	676734	1.361	0.238	0.167
		fine	0.01	0.228	889574	1.357	0.235	0.166
	Curved cyl	coarse	0.06	0.457	1953096	1.424	0.316	0.167
		medium	0.03	0.457	3975792	1.399	0.289	0.166
		fine	0.01	0.228	5851477	1.394	0.287	0.166
500	Straight cyl	coarse	0.01	0.571	723109	1.241	0.371	0.203
		medium	0.008	0.457	876734	1.235	0.364	0.201
		fine	0.004	0.228	1089574	1.228	0.358	0.202
	Curved cyl	coarse	0.008	0.457	2453096	1.338	0.564	0.205
		medium	0.008	0.457	4175792	1.317	0.556	0.204
		fine	0.004	0.228	6051477	1.310	0.549	0.204

Table 2

Comparisons of the numerical and experimental results of a straight cylinder from medium mesh with other numerical and experimental results at $Re = 100$ and 500.

Re	Studies	$\overline{C_D}$	C'_L	St
100	Present (medium)	1.361	0.238	0.167
	Numerical results			
	Meneghini et al. (2001)	1.370	—	0.165
	Braza et al. (1986)	1.364	0.181	0.160
	Kang et al. (1999)	1.340	0.236	0.164
	Sharman et al. (2005)	1.320	0.230	0.164
	Kang (2003)	1.330	0.320	0.165
	Stansby and Slaouti (1993)	1.317	0.248	0.166
	Muddada and Patnaik (2010)	1.40	0.240	0.170
	Burbau and Sagaut (2002)	1.410	0.257	0.164
	Experimental results			
	Clift et al. (1978)	1.33	0.167	
	Williamson (1989)		0.164	
	Hammache and Gharib (1991)		0.166	
	Norberg (1994)		0.165	
	Schlichting and Gersten (2003)	1.502 ^a	0.202	
	Norberg (2003)			
500	Present (medium)	1.235	0.364	0.201
	Numerical results			
	Batcho and Karniadakis (1991)	1.160	—	0.200
	Mittal and Balachandar (1995)	1.240	—	—
	Thapa et al. (2015)	1.202	0.356	0.203
	Experimental results			
	Schlichting and Gersten (2003)	1.219 ^b		
	Norberg (2003)		0.204	

^a Value at $Re = 111$.

^b Value at $Re = 473$.

$$C_L = \frac{2F_L}{\rho AU^2} \quad (4)$$

$$\overline{C_p} = \frac{2(P - P_\infty)}{\rho U^2} \quad (5)$$

$$St = \frac{f_s D}{U} \quad (6)$$

where F_D and F_L are the drag and lift forces on a straight cylinder in the in-line and cross-flow directions, respectively, and they are calculated by integrating the pressure and shear stress around the surface of the cylinder. $\overline{C_p}$ is the mean pressure coefficient, P_∞ is the pressure at the inlet boundary, A is the projected area of the curved cylinder in the flow direction, calculated as $A = (R+D/2+L_v)D$. f_s is the vortex shedding frequency, which is obtained by performing the fast Fourier transform (FFT) analysis of the lift coefficient.

Fig. 2 shows the time histories of the lift and drag coefficients for the vertical extension of the single curved cylinder calculated from the coarse, medium and fine meshes at $Re = 100$ and 500. It can be seen that both the lift and drag coefficients from the medium and fine meshes agree well with each other at $Re = 100$. At $Re = 500$, due to the three-dimensionality of the flow, the fluctuations of the force coefficients behave not regularly periodic, the results from the medium mesh are in consistent with those from the fine mesh. As shown in Table 1, the mean drag coefficient $\overline{C_D}$ and Strouhal number St for the straight cylinder from the medium mesh are nearly the same as the values from the fine mesh at $Re = 100$. The difference between the root-mean-square lift coefficients C'_L of the medium and fine meshes is less than 1.3% for the straight cylinder with the length of $H = 6D$ at $Re = 100$. The differences in $\overline{C_D}$ and C'_L between the medium and fine meshes are about 0.4% and 0.7% between the medium and fine meshes for the vertical extension of the curved cylinder, respectively. At $Re = 500$, for the straight cylinder, the percentage changes of $\overline{C_D}$ and St are less than 0.6% and 0.5% between the medium and fine meshes, respectively. While the variation of C'_L is

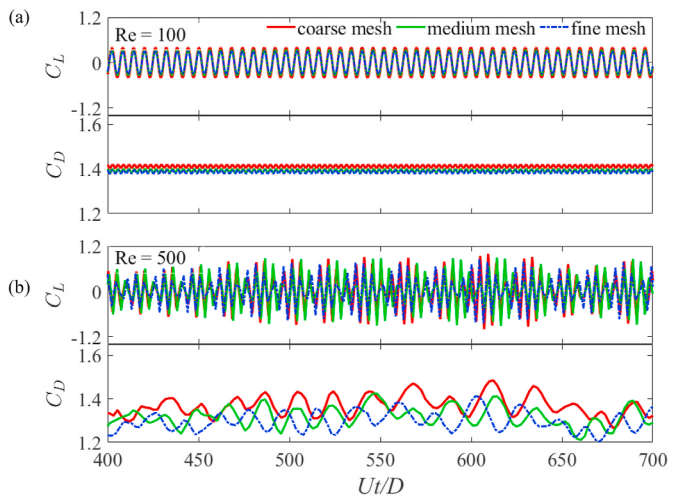


Fig. 2. Time histories of force coefficients for a single curved cylinder without vertical extension: (a) $Re = 100$; (b) $Re = 500$.

approximately 1.7% for both cases. The mesh refinement from medium to fine leads to 0.5% decreasing in $\overline{C_D}$ and 1.3% decreasing in C'_L for the vertical extension of the curved cylinder. Therefore, the medium mesh density is considered to be sufficient to obtain accuracy results for flow past two side-by-side curved cylinders.

The $\overline{C_D}$ of the straight cylinder from the medium mesh agree with the results of Meneghini et al. (2001) and Braza et al. (1986) for $Re = 100$, and the present results of C'_L and St agree well with the published results. It is observed that the C'_L of the curved cylinder obtained from the mid-span of the straight vertical extension are larger than the results of the straight cylinder, while the $\overline{C_D}$ agrees well with the results of Muddada and Patnaik (2010) and Burbau and Sagaut (2002). As for $Re = 500$, the $\overline{C_D}$ and St of the straight cylinder obtained from the medium mesh are in good agreement with the results of Batcho and Karniadakis (1991), Mittal and Balachandar (1995), and Thapa et al. (2015). The difference of C'_L between the present simulation and published results is less than 2.2%.

Fig. 3 shows the wake topology for flow past a single curved cylinder at $Re = 100$ and 500. It can be seen that at $Re = 100$, the shed vortex cores are straight in the wake of the vertical straight section and distorted further downstream this section. As Re increases to 500, the wake flow exhibits three-dimensional wake instabilities, many small rib-shaped streamwise vortical structures are observed and the vortical structures along the span of the curved cylinder become more energetic. The present results of wake topologies agree well with those reported in Miliou et al. (2007). The time-averaged flow is obtained by averaging the flow fields from $Ut/D = 400$ to 700 and the streamlines of time-averaged flow are presented in Fig. 4. It can be seen that the time-average streamlines are parallel to the free stream in the downstream of the curved cylinder, but distorted near the curved segment due to the effect of the curvature. The recirculation zone near the rear stagnation line gradually decreases along the cylinder span, which is in good agreement with those in Canabes (2010). Fig. 5 shows the comparisons of the mean pressure coefficient and time-averaged flow velocity in the z-direction along the span of the convex configuration for flow past a single curved cylinder at $Re = 100$ and 500 with the published literature results. The time-averaged flow velocity in z-direction along the span is extracted 0.3D upstream of the front stagnation line of the curved cylinder. The variation trend of the absolute values of the base pressure coefficients along the span of the curved cylinder is in good agreement with those of Miliou et al. (2007) and Zhu et al. (2018). The discrepancies between the present result of $\overline{C_{ps}}$ and that of Canabes (2010) may be caused by the adoption of different computational

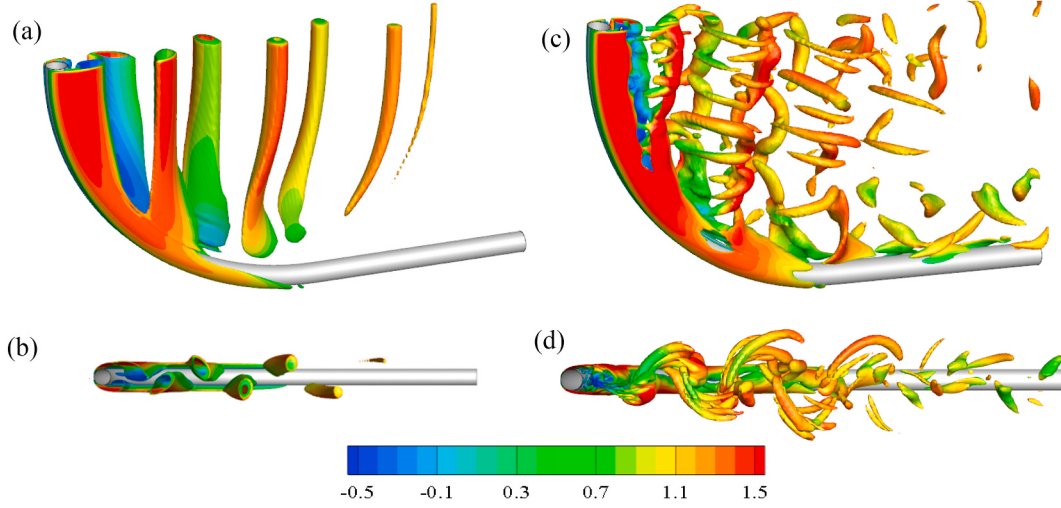


Fig. 3. The present results of the three-dimensional wake topology and top view of the wake topology: (a)–(b) $Re = 100$, (c)–(d) $Re = 500$.

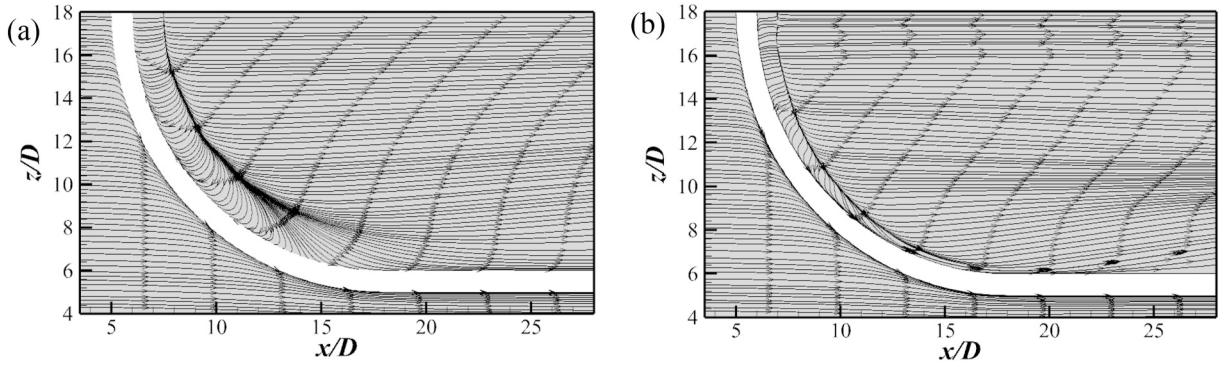


Fig. 4. The present results of time-averaged streamline topology: (a) $Re = 100$, (b) $Re = 500$.

domains. The non-dimensional time-averaged flow velocity along the span \bar{w}/U_{∞} shows firstly an increasing and then decreasing trend with the increase of s/D , and reaches to the minimum value at $s/D = 10$. The variations of the flow velocities with s/D are in good agreement with those of Miliou et al. (2007) and Lee et al. (2020).

To further validate the present numerical method, the comparisons of the mean stagnation pressure coefficients on the vertical cylinder surfaces for flow past a straight cylinder between the present numerical study and literature results are performed and the variation of the mean stagnation pressure coefficient \bar{C}_p for a single straight cylinder with Reynolds number is plotted in Fig. 6. It can be seen that the mean stagnation pressure coefficient decreases with the increase of Reynolds number. The \bar{C}_p for the straight cylinder in the present study is in good agreement with the variation trend of the fitted curve and the literature results (Batham, 1973; Canabes, 2010; Homann, 1936; Kravchenko and Moin, 2000; Lei et al., 2001; Norberg, 1994; Rajani et al., 2009; Thom, 1933).

4. Numerical results

4.1. Instantaneous wake flow patterns

The instantaneous vortex flow structures at different spacing ratios ($1.25 \leq L/D \leq 5.0$) and Reynolds numbers ($100 \leq Re \leq 500$) at $Ut/D = 650$ are presented in Fig. 7, and the top views of these three-dimensional vortex tubes at the x - y plane are also depicted in Fig. 8. The non-dimensional vortices iso-surfaces are identified by the Q -criterion $Q =$

$\frac{1}{2}(\|\Omega\|^2 - \|S\|^2)$, where the Ω and S are the anti-symmetric and symmetrical parts of the velocity gradient tensor, respectively. The non-dimensional Q^* is defined as $Q^* = QD^2/U^2$. The wake flow pattern behind two curved cylinders varies significantly along the span, similar to those for a single curved cylinder (Gallardo et al., 2014a,b; Shang et al., 2018). Both the spacing ratio and Reynolds number have significant effects on the three-dimensional wake flow topologies for two curved cylinders.

At small spacing ratio of $L/D = 1.25$, two curved cylinders are in a close proximity regime, where only one pair of vortex tubes is formed in the wake and the two cylinders behave as a single bluff body. Behind the vertical parts of two curved cylinders, the shear layers roll up and form a single vortex street with large scale vortex tubes behind two cylinders. At $Re = 100$, the primary vortex tubes are nearly parallel to the curved axis, and the wake width along the curved sections of two cylinders decreases. Due to the phase difference of vortex shedding along the cylinder span, the vortices $Re = 300$ and 500 become inclined. With the increase of the Reynolds number, the waviness of the wake flow is observed behind two side-by-side curved cylinders and the streamwise vortices becomes stronger. As L/D increases to 1.5, the vortex dislocation is observed at the junction of the vertical and curved sections of two cylinders. The dislocation of the primary vortices is caused by the Mode A wake, which occurs at higher Reynolds number for straight cylinders. The continuities of the vortex cores are obviously destroyed and the wake flow becomes less coherent along the span. Although the spanwise vorticities are wavy at high Reynolds number, they are perpendicular to the incoming direction at $Re = 300$ and parallel to the upper part of the curved cylinder at $Re = 500$. This is similar to flow past a straight

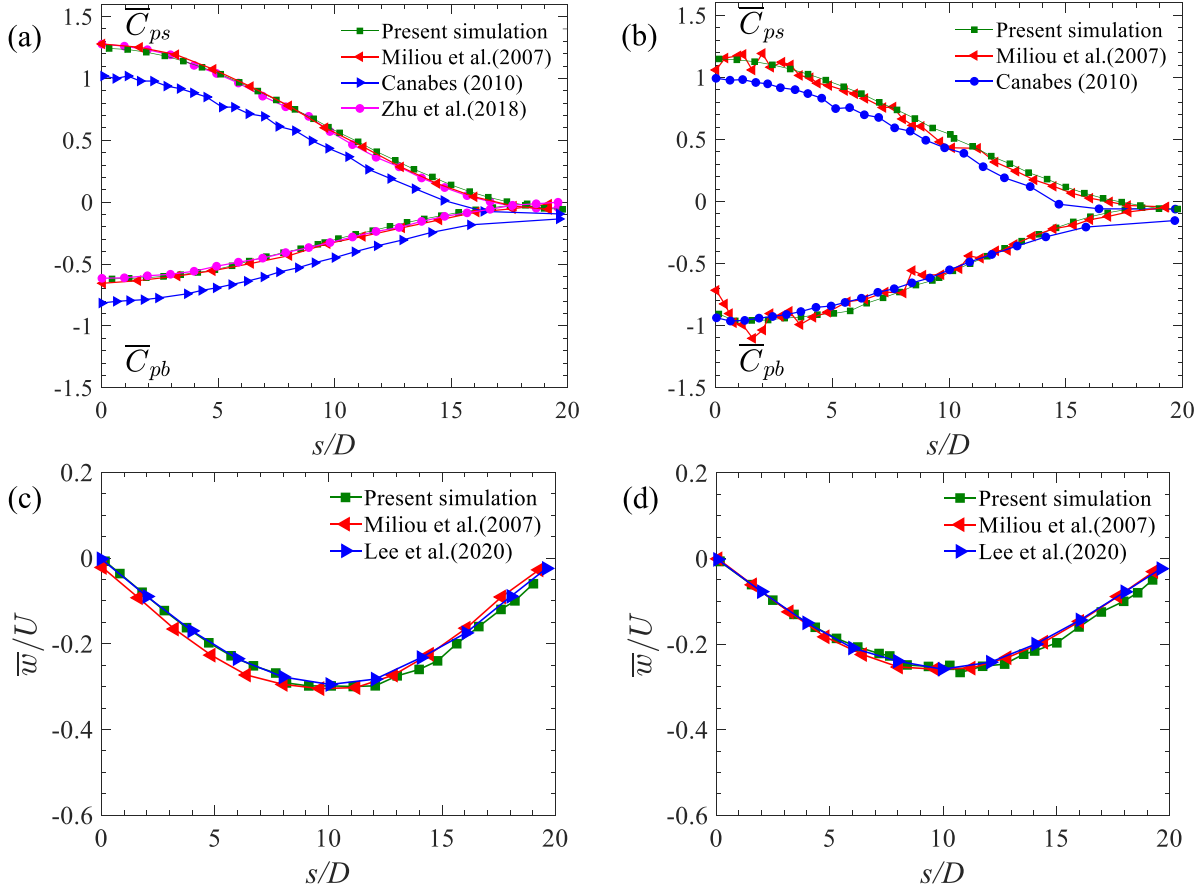


Fig. 5. Comparisons of the results for the mean pressure coefficient and velocity along the span of the convex configuration among the present numerical result with published literatures: (a) \bar{C}_p at $Re = 100$, (b) \bar{C}_p at $Re = 500$, (c) \bar{w}/U at $Re = 100$, (d) \bar{w}/U at $Re = 500$.

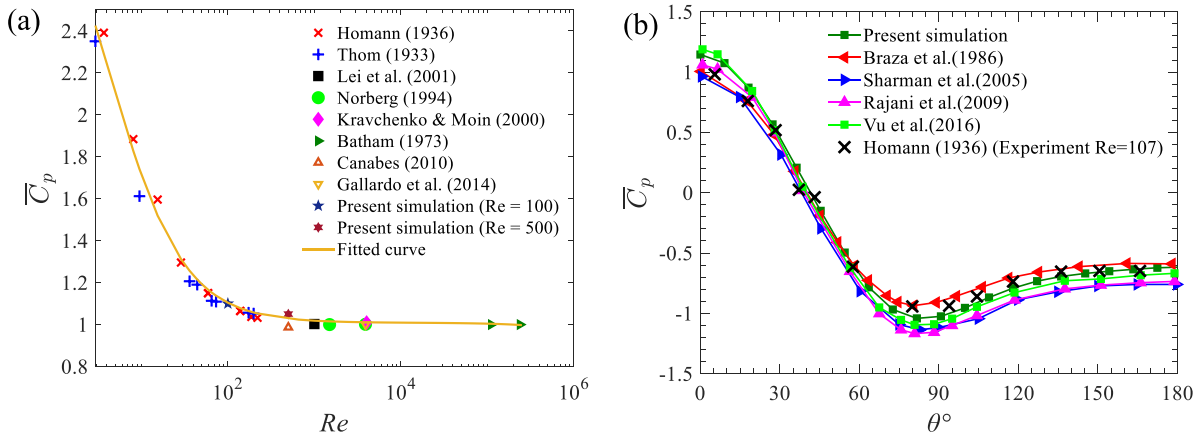


Fig. 6. Comparisons of the results for the mean pressure coefficient for the vertical cylinder between the present simulation with published literatures: (a) mean stagnation pressure coefficients at different Reynolds numbers, (b) mean pressure coefficients at $Re = 100$.

inclined cylinder, where the wake vortices are always parallel to the cylinder (Zhao et al., 2013).

As L/D is increased to 2, the spanwise vortex tubes are twisted at the junction of the vertical and the curved section for $Re = 100$, where the spanwise vortices are inclined and weak. The scales of the vortex tubes generated from the curved part of the cylinder decrease. As Re increases to 300 and 500, the wake flow is weakly turbulent. The energy is transferred from the spanwise vortices to the streamwise vortices that dissipates quickly. The location of the primary vortex moves towards to

the surface of curved cylinders and the small vortices are amalgamated to form a cluster of vortical structures near the horizontal extension. The vortex tubes behind the vertical extension are parallel to the cylinder, the shape of vortex tubes remains parallel to the axis of the cylinder at lower part of the curved section.

At large spacing ratios of $3 \leq L/D \leq 5$, symmetric vortex shedding is observed in the wake of the vertical extensions of two curved cylinders for $Re = 100$ in Figs. 7 and 8. Two vortex tubes that are shed from the cylinder are parallel to the vertical section of the cylinder, indicating the

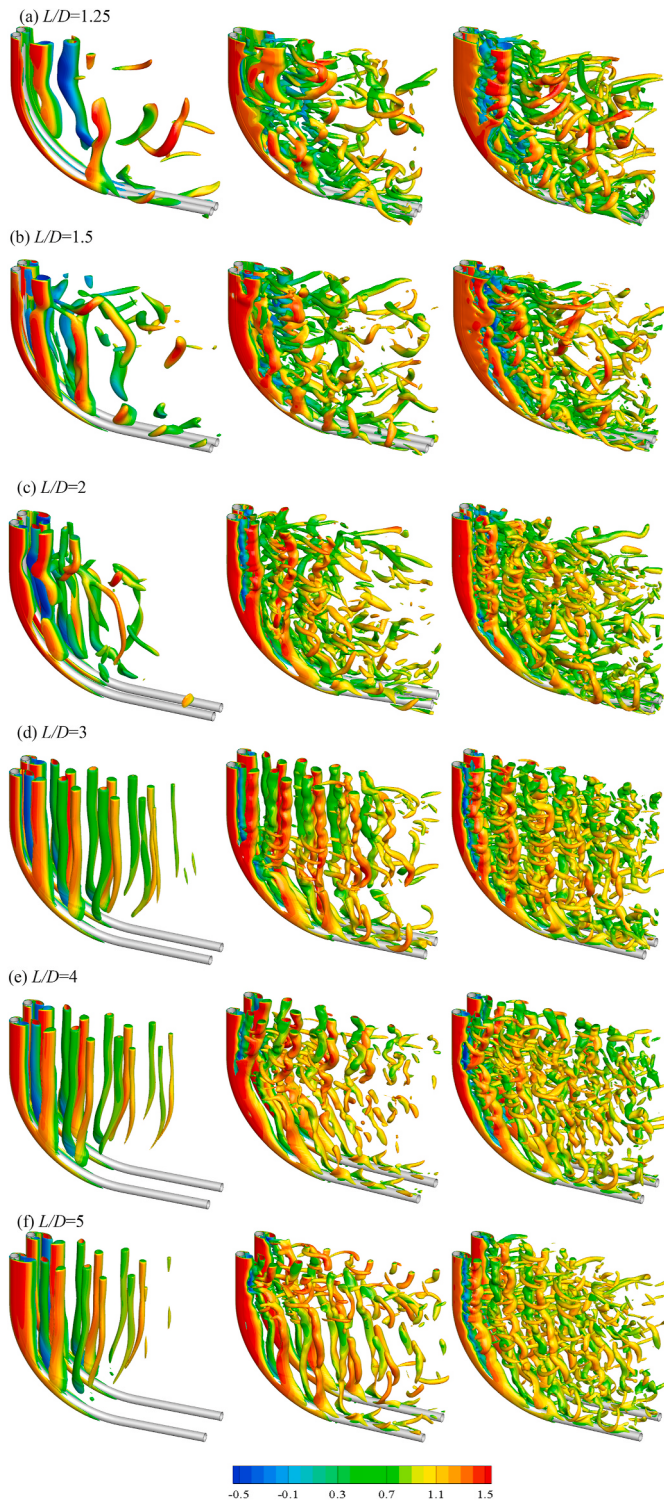


Fig. 7. Instantaneous iso-surfaces of $Q^* = 0.15$ for different Reynolds numbers at $Ut/D = 650$: (a) $L/D = 1.25$, (b) $L/D = 1.5$, (c) $L/D = 2$, (d) $L/D = 3$, (e) $L/D = 4$, (f) $L/D = 5$. From left to right columns: $Re = 100$, $Re = 300$, $Re = 500$.

two-dimensional flow for the vertical extension at $Re = 100$. The two curved cylinders behave more independent at $Re = 100$. On the lower sides of two curved cylinders, the axial flows are directed towards the vertical extensions, vortex shedding is vanished close to the horizontal extensions. The wavy primary vortices are parallel to the axis of the vertical segment of two curved cylinders. The distortion of the spanwise vortices and the generation of the strong streamwise vortices are

observed behind the vertical segment, similar to the wake flow of Mode B for flow past a vertical cylinder (Williamson, 1988; Barkley and Henderson, 1996). The vortical structure at the curved parts of two cylinders become more enhanced, the coherence of the wake caused by the alternating primary vortices disappears. The vorticity structures are moved towards to the surfaces of two cylinders, leading to the oblique shedding phenomenon in the wake of the curved segments. On the other hand, the non-shedding regime at $Re = 100$ and the shear layer instabilities for $Re = 300$ and 500 are observed close to the horizontal extension.

The wake flow behaviors behind two side-by-side curved cylinders are further investigated by studying the instantaneous non-dimensional vorticity contours at different horizontal sections of two curved cylinders with $Re = 100$ and 300 shown in Fig. 9. The non-dimensional instantaneous spanwise vorticity ω_z^* is defined as $\omega_z^* = \omega_z D/U$, where $\omega_z = \partial v / \partial x - \partial u / \partial y$. When $L/D = 1.25$, a single vortex street is observed along the vertical parts of the cylinder span of two curved cylinders for $Re = 100$ and 300. It is interesting to note that the deflected gap flow is observed at $Re = 300$, where a narrow wake and a wide wake are formed behind two curved cylinders. The inner vortices developed in the gap flow are squeezed and merged with the shed vortices on the outer sides of the cylinders, resulting in a single large scale vortex street formed in the downstream wake.

The flow feature for $L/D = 1.5$ is the same as that for $L/D = 1.25$. It is interesting to note that different from those of two side-by-side straight cylinders, the switchover of the gap flow deflection occurs along the curved spans for two curved cylinders at $Re = 100$ and 300. The phase differences of vortex shedding along the cylinder span cause the inclination of the spanwise vortices and result into the oblique vortex shedding pattern. At low Reynolds number $Re = 100$, depending on the deflected direction of the gap flow, the asymmetrical wake flow pattern with a narrow and a wide wake is observed at the upper part of the vertical extension $z/D = 27.5-17.5$. At the lower side close to the horizontal plane $z/D = 12$, the shear layers become parallel to the incoming flow direction with the suppression of vortex shedding process. As Re increases, the switchover of the gap flow deflection occurs at $z/D = 17.5$ and 12.

With the increase of L/D to 2, two parallel vortex streets are observed along both the curved and vertical straight spans with the coupling vortices formed behind two cylinders, which could be regarded as the dual vortex street regime. Different from the cases of two straight cylinders, a distinct flow feature of the transition from the in-phase to the anti-phase vortex shedding pattern is observed along the curved spans of two cylinders. Take the case of $Re = 300$ for example, at the upper part of vertical extension $z/D = 27.5$, the vortex shedding is predominantly in the in-phase pattern, where the vortices with the same rotational signs are synchronized shed behind two cylinders. The shed vortices become weakened due to the interactions of the vortices with opposite signs.

At the lower part close to the horizontal extension $z/D = 12$, the anti-phase vortex shedding occurs behind two cylinders, where the vortices are shed synchronized in the opposite directions. As L/D increases to 3, the proximity interference between two cylinders becomes weak and each cylinder behaves like an isolated bluff body. Two parallel shed vortices in the anti-phase and in-phase patterns are observed along the curved span. The vortices observed at the upper and lower parts are out of phases, where two rows of parallel shed vortices are predominantly in the anti-phase pattern at $z/D = 22.5$ and 27.5 and changes to in-phase pattern at the lower side horizontal planes $z/D = 17.5$ for $Re = 100$. At $z/D = 12$, the large inclination suppresses the vortex shedding and the shear layers separated from two cylinders are stretched, no regular vortex shedding is observed. The three-dimensionality of the wake flow behind two side-by-side curved cylinders are enhanced at $Re = 300$, the regular in-phase vortex shedding is observed at all the examined horizontal planes for $L/D = 3$.

The streamwise evolutions of the wake behind the horizontal ex-

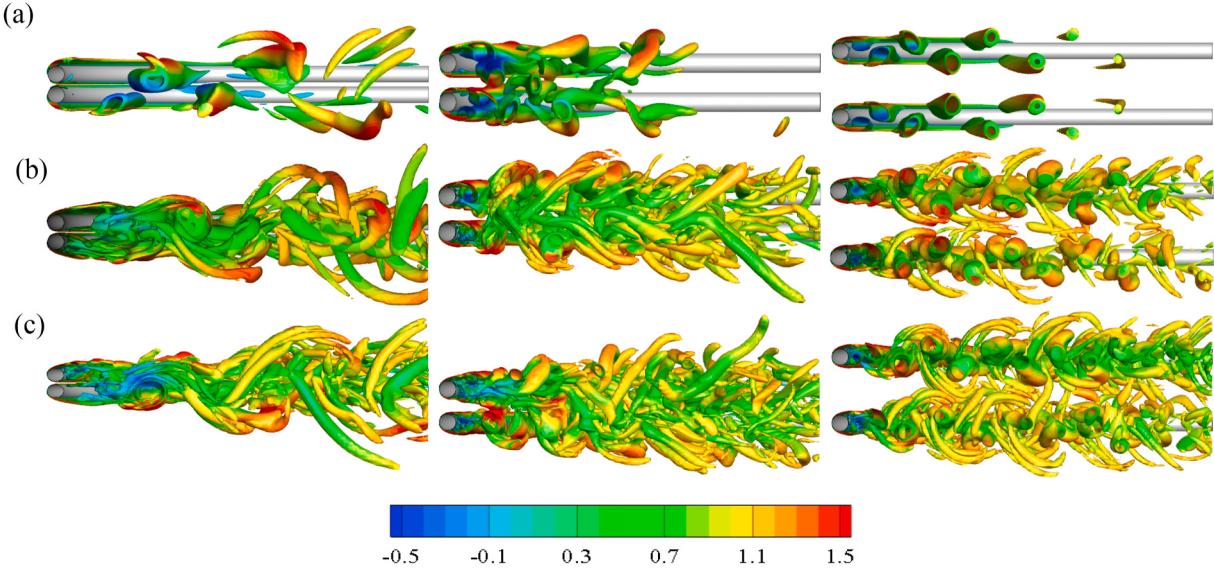


Fig. 8. Instantaneous iso-surfaces of $Q^* = 0.15$ at $Ut/D = 650$: (a) $Re = 100$, (b) $Re = 300$, (c) $Re = 500$, from left to right columns: $L/D = 1.25$, $L/D = 2$, $L/D = 4$.

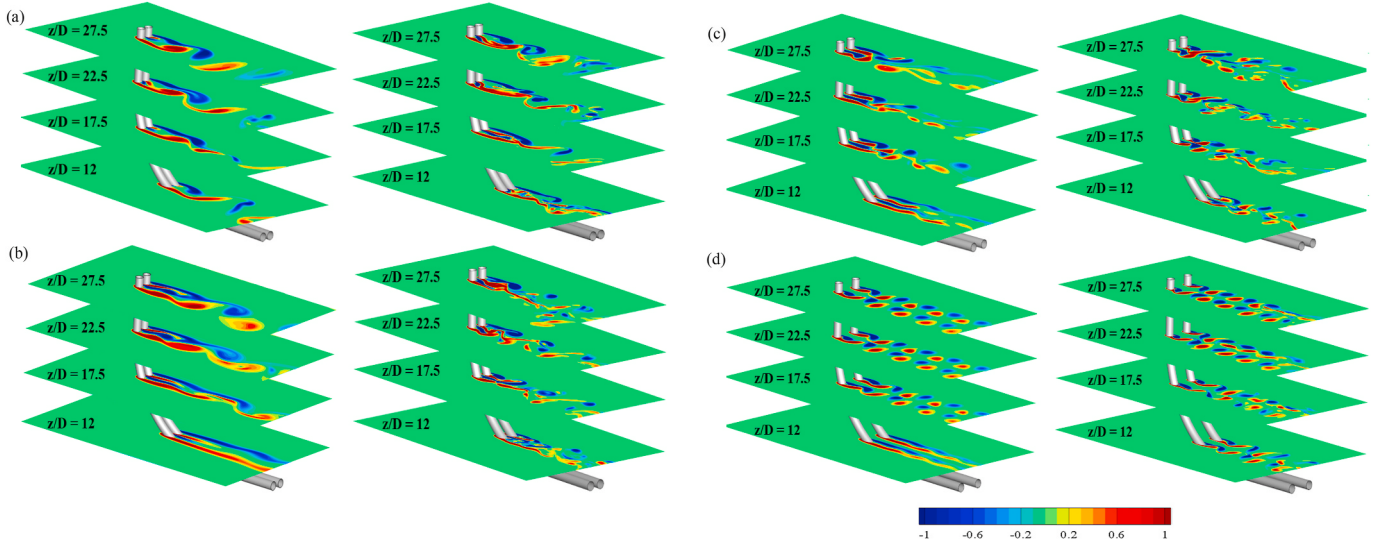


Fig. 9. Instantaneous vorticity contours at different (x - y) planes: (a) $L/D = 1.25$, (b) $L/D = 1.5$, (c) $L/D = 2$, (d) $L/D = 3$. Left column: $Re = 100$, right column: $Re = 300$.

tensions of two curved cylinders are also illustrated. Fig. 10 shows the non-dimensional instantaneous vorticity contours ω_x^* at different vertical (y - z) planes at different spacing ratios $1.25 \leq L/D \leq 3$ and Reynolds numbers $Re = 100$ and 300 . The non-dimensional instantaneous streamwise vorticity ω_x^* is defined as $\omega_x^* = \omega_x D/U$, where $\omega_x = \partial w / \partial y - \partial v / \partial z$. It is interesting to note that the wake flow patterns are significantly affected by the Reynolds numbers and spacing ratios, behave different along the spans of horizontal extensions for two curved cylinders. At the vertical plane $x/D = 12$, close to the vertical segment of two curved cylinders, two counter-rotating vortices evolve along the axis of each curved cylinder. For low Reynolds number $Re = 100$, the two cylinders behave as a single bluff body at $L/D = 1.25$, an alternate vortex shedding is observed at the further downstream location $x/D = 28$. As L/D increases to 1.5 , an asymmetrical wake flow pattern is also observed in the streamwise vorticity contours. As L/D increases to 3.0 , the anti-phase vortex shedding mode is observed along the horizontal extension spans of two cylinders. With the increase of Re , the streamwise wake flow exhibits high turbulence, and the intense of the vortices

increases.

4.2. Time-averaged flow characteristics

Fig. 11 shows the time-averaged streamlines at different spanwise locations in the x - y planes with different spacing ratios behind two side-by-side curved cylinders for $Re = 300$. The time-averaged streamline topologies are obtained by averaging the velocity and pressure over the time period $400 \leq Ut/D \leq 700$, where the gap flow is only biased to one cylinder behind the vertical straight section at $1.25 \leq L/D \leq 1.5$. At $L/D = 1.25$, the gap flow is deflected downwards, resulting into an asymmetrical streamline pattern. A large scale of recirculation zone is formed behind C1 and a small scale of recirculation zone is formed behind C2. The streamlines in the downstream are distorted due to the proximity interference between two cylinders. Due to the curvatures of two curved cylinders, the variation of the streamwise velocity along the span direction is irregular. The scale of the recirculation zone gradually decreases from $z/D = 27.5$ to $z/D = 17.5$. As L/D increases to 2 and 3, the

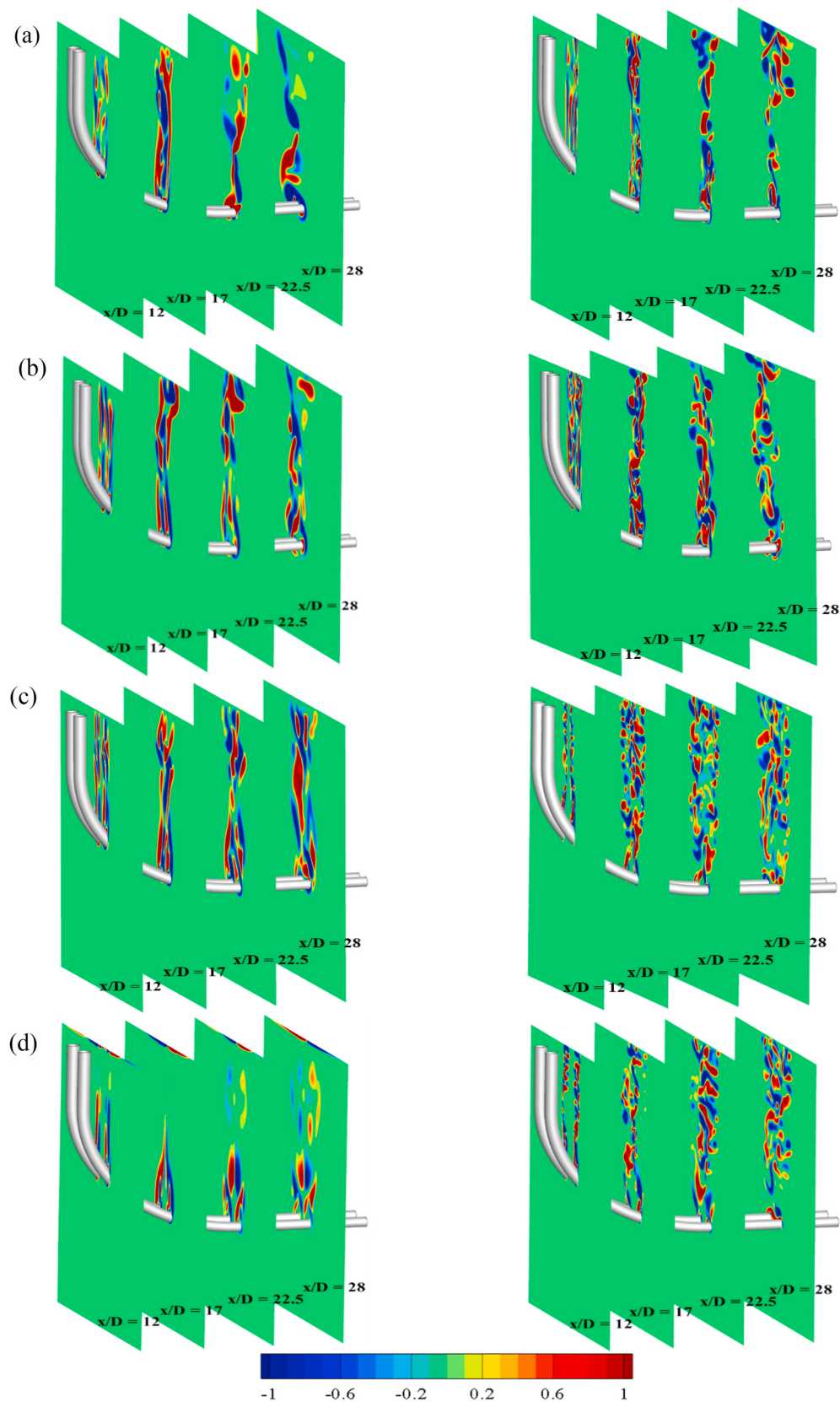


Fig. 10. Instantaneous vorticity contours at different $(y-z)$ planes: (a) $L/D = 1.25$, (b) $L/D = 1.5$, (c) $L/D = 2$, (d) $L/D = 3$. Left column: $Re = 100$, right column: $Re = 300$.

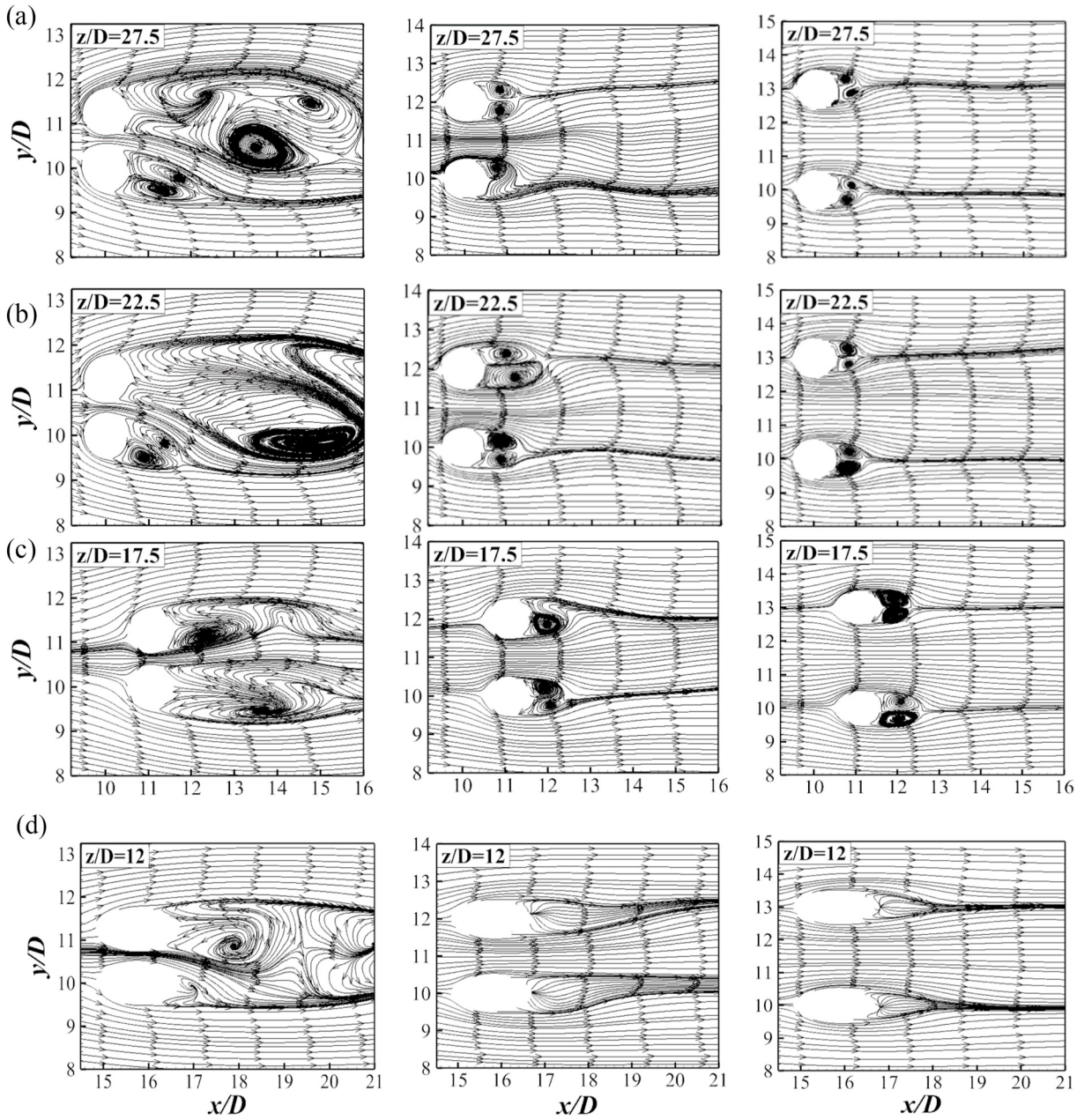


Fig. 11. Time-averaged velocity streamlines topology at different spanwise locations for $Re = 300$: (a) $z/D = 27.5$, (b) $z/D = 22.5$, (c) $z/D = 17.5$, (d) $z/D = 12$. Left column: $L/D = 1.25$, mid column: $L/D = 2$, right column: $L/D = 3$.

streamline topologies between two curved cylinders become parallel and regular at the horizontal plane $z/D = 12$, the recirculation zone disappears. At $L/D = 2$ and 3, the scale of the reverse flow zone behind each curved cylinder decreases, and is approximately symmetrical with the centerline between two cylinders at different spanwise locations.

The contours of the time-averaged Reynolds stresses $\overline{u'v'}/U^2$, $\overline{v'v'}/U^2$ and Reynolds shear stress $\overline{u'v'}/U^2$ at different z/D locations for $L/D = 1.25, 2$ and 3 with $Re = 300$ are presented in Figs. 12–14, where the positive and negative values are represented by solid and dashed lines, u' and v' are the root mean square velocities in the x - and y -directions, respectively. With the increase of L/D , different Reynolds stress characteristics are observed along the spans of two curved cylinders. At small spacing ratio $L/D = 1.25$, the Reynolds stress contours exhibit asymmetrical distribution, a small Reynolds normal stress contour $\overline{u'u'}/U^2$ exists behind two cylinders. The Reynolds stress intensity decreases along the span of curved cylinders, in consistent with the

variations of vortices strengths. The Reynolds normal stress contour $\overline{v'v'}/U^2$ exhibits a single peak causing by the vortex shedding. With the increase of L/D to 2 and 3, the Reynolds stress distributions at $z/D = 27.5, 22.5$ and 17.5 for two side-by-side curved cylinders are similar to that of a single cylinder. The Reynolds normal stress and Reynolds shear stress contours are symmetric and anti-symmetric with the centerline between two curved cylinders, respectively. The amalgamation phenomena of the inner Reynolds normal stress contours are observed between two curved cylinders. The intensity of the Reynolds normal stress $\overline{u'u'}/U^2$ reaches to the maximum value at $x = 1.5D$ downstream of the cylinder. Two small lobes are observed in the Reynolds shear stress contour $\overline{u'v'}/U^2$ in the upstream and two large lobes in the downstream. No Reynolds shear stress contour is observed close to the rear of cylinder, which may be contributed to the little fluctuations of the velocity in the x - z plane in the wake (Dong et al., 2006).

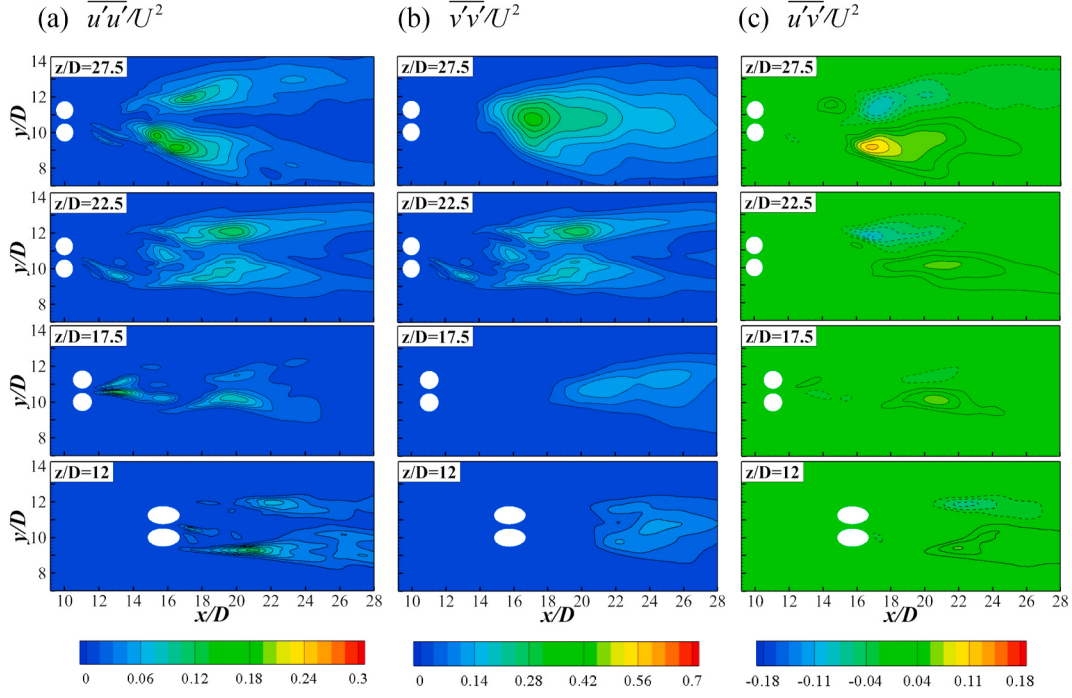


Fig. 12. Reynolds stress contours at $L/D = 1.25$ for $Re = 300$: (a) $\overline{u'u'}/U^2$, (b) $\overline{v'v'}/U^2$, (c) $\overline{u'v'}/U^2$.

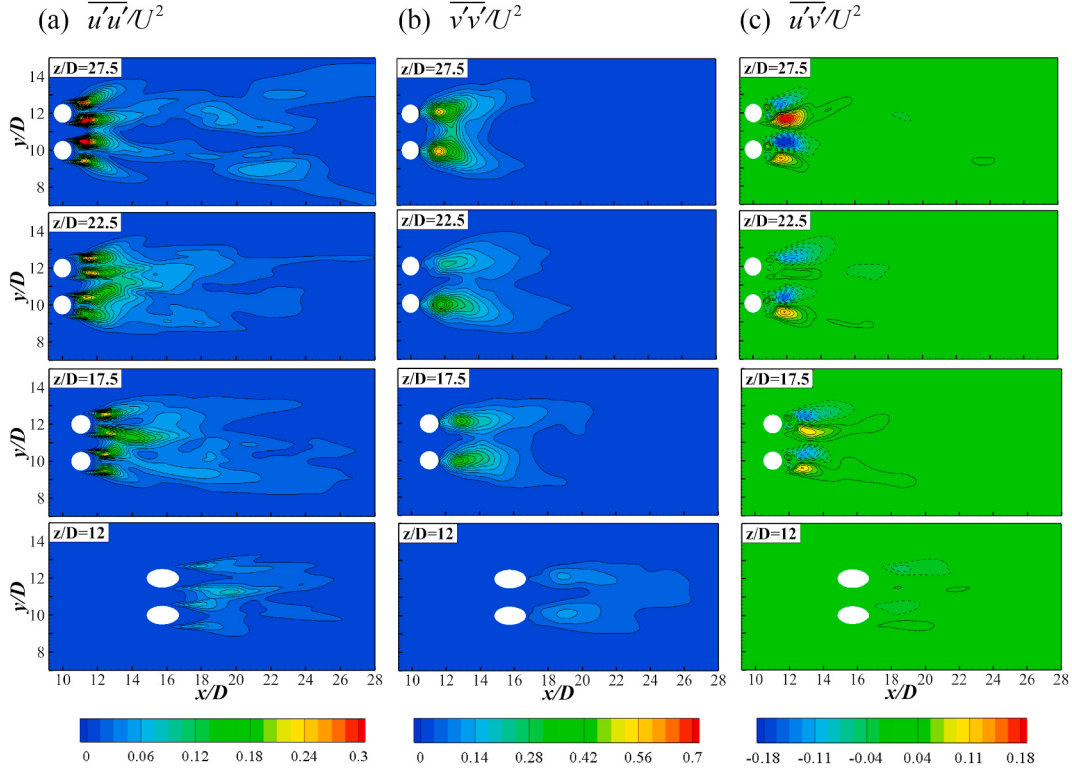


Fig. 13. Reynolds stress contours at $L/D = 2$ for $Re = 300$: (a) $\overline{u'u'}/U^2$, (b) $\overline{v'v'}/U^2$, (c) $\overline{u'v'}/U^2$.

4.3. Axial flow characteristics

Figs. 15 and 16 show the contour plots of the mean streamwise velocity \bar{u} and vertical velocity \bar{w} at two (x, z) -slices (i.e. $y/D = 10$ and $y/D = 10 + L/D$) for different spacing ratios $L/D = 1.25, 2, 3$ and $Re = 300$. The curvature has a significant effect on the flow velocity distributions along the span of two side-by-side cylinders. A recirculation zone is

observed in front of the vertical and curved segments for two cylinders, where the values of \bar{u} and \bar{w} are negative. The flow direction shifts counterclockwise in the horizontal extension along the curved span, the vertical component gradually increases and finally aligns with the incoming flow velocity. The scale of recirculation zone decreases with increasing of L/D . The length of the reverse flow zone in the streamwise direction is significantly reduced. The mean streamwise velocities

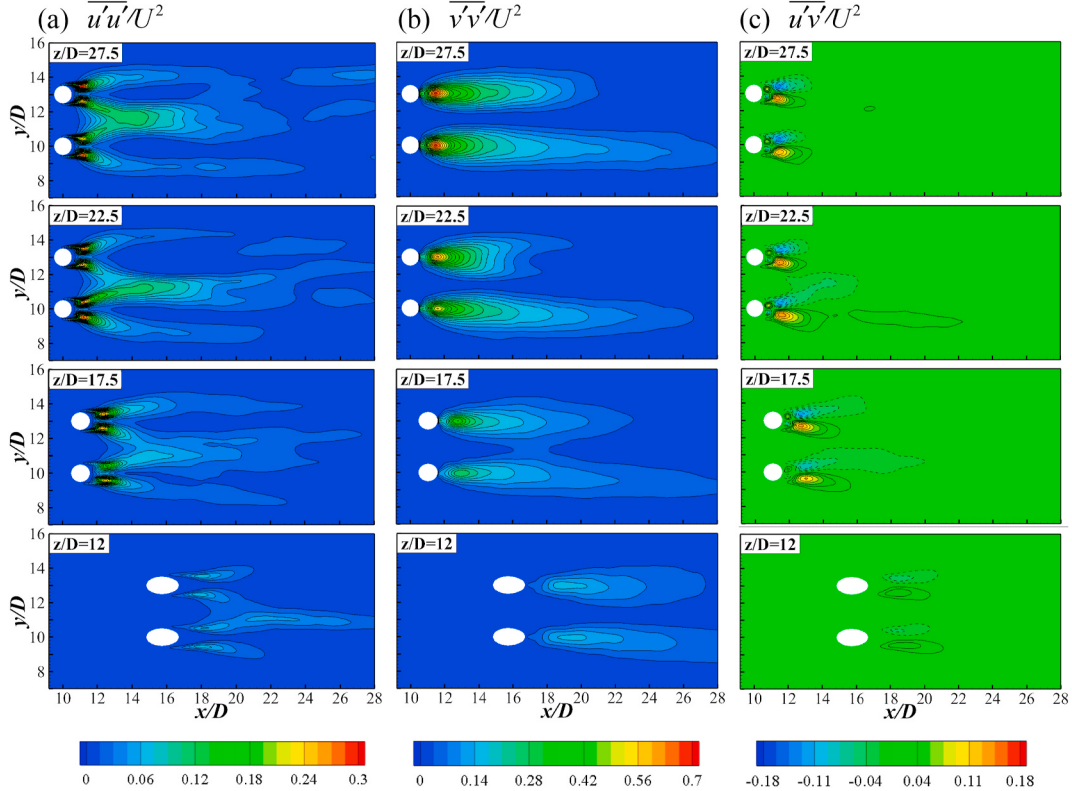


Fig. 14. Reynolds stress contours at $L/D = 3$ for $Re = 300$: (a) $\overline{u'u'}/U^2$, (b) $\overline{v'v'}/U^2$, (c) $\overline{u'v'}/U^2$.

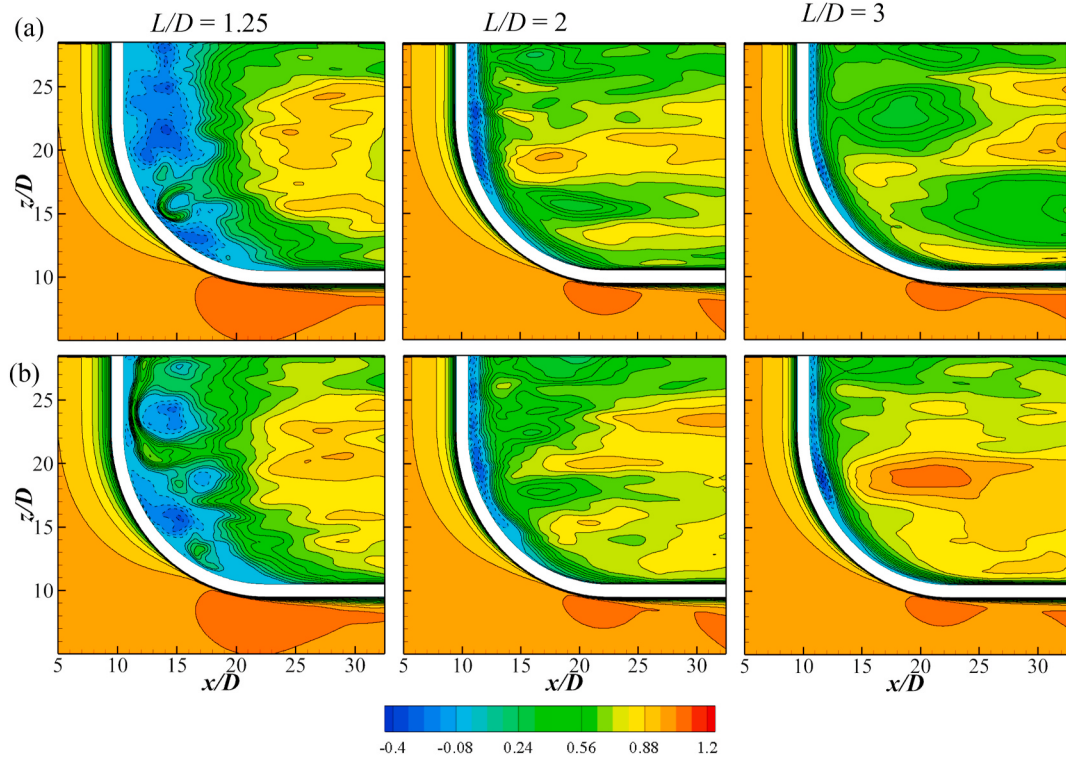


Fig. 15. Iso-contours of time-averaged streamwise velocity at two (x, z)-slices: (a) C1, (b) C2. Left column: $L/D = 1.25$, mid column: $L/D = 2$, right column: $L/D = 3$.

gradually decrease as approaching to the surface of the curved cylinders. The distribution of the spanwise velocity near the curved section of two cylinders exhibits a similar trend to that of a single curved cylinder. The spanwise velocity is negative at both the front and rear of the curved

segment, and positive at the rear of the vertical extension. With the increase of L/D , the scale of the recirculation zone decreases, where the spanwise velocity is negative, the reverse flow is suppressed at the location close to the horizontal extension.

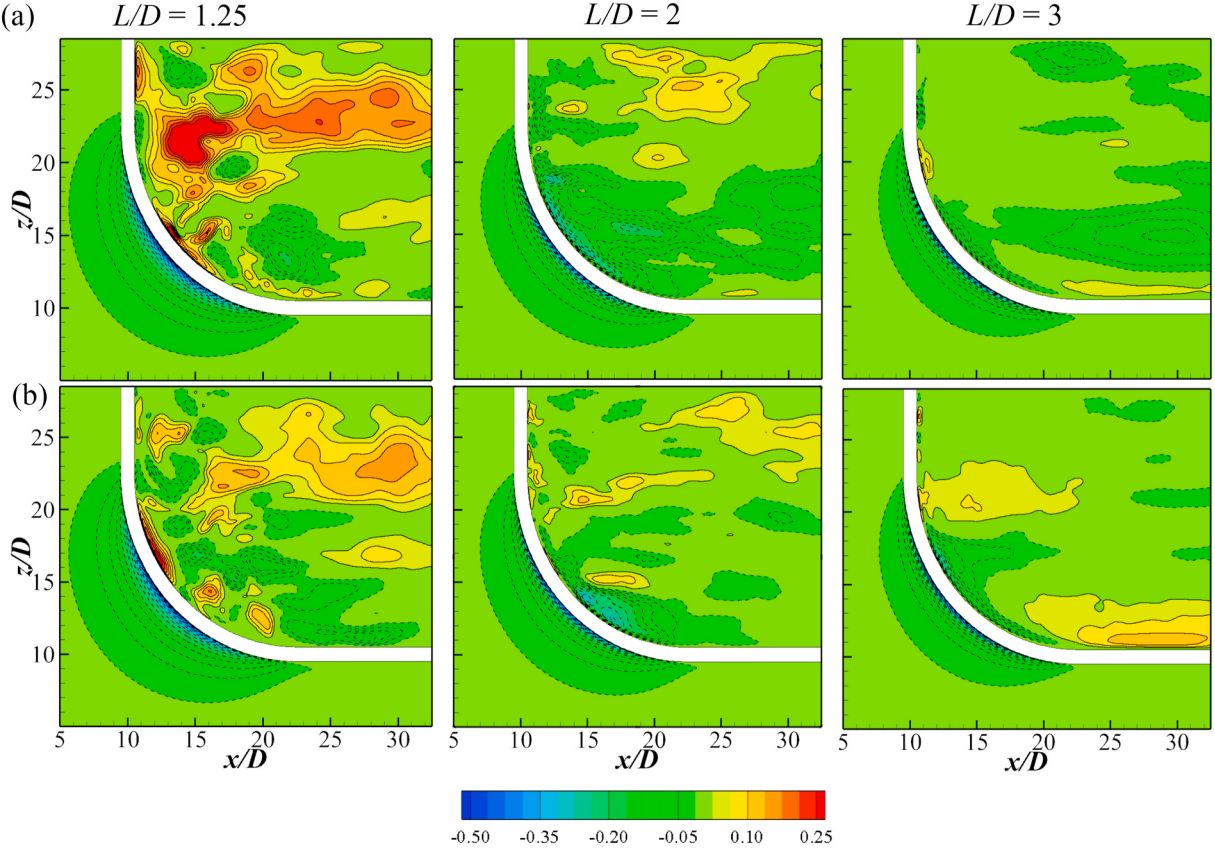


Fig. 16. Iso-contours of time-averaged vertical velocity \bar{w} at two (x, z) -slices: (a) C1, (b) C2. Left column: $L/D = 1.25$, mid column: $L/D = 2$, right column: $L/D = 3$.

The contours of \bar{w} depict an upwards and downwards flow in upper and lower part of two curved cylinders, respectively. With the increase of the depth, the three-dimensionality of the flow can be illustrated by the profiles of mean vertical velocity \bar{w} . At $z/D = 27.5$ and 22.5 , the profile exhibits an upwelling flow from the axial curvature of two curved cylinders propagating upwards along the vertical extension. The vertical velocity close to the horizontal extension reaches to $0.2U$. Further downstream, the profiles of \bar{w} at $z/D = 17.5$ and 12 exhibit a downdraft flow, where the downdraft vertical velocity increases with depth and reaches almost 20% of the free-stream velocity U at the curved parts of two cylinders.

Fig. 17 plots the time-averaged axial velocity \bar{u}_{ax} distribution along a line behind each cylinder surface at different spacing ratios and Reynolds numbers, the line is defined as a curve parallel to the curved cylinder with offset of $1.1D$, as shown in Fig. 17(c). Following Jiang et al. (2018, 2019), the axial velocity u_{ax} used in the present study is defined as the local tangential velocity along the curved cylinder and calculated based on the streamwise velocity u and vertical velocity w , $u_{ax} = u \sin \phi + w \cos \phi$. When the u_{ax} increases, the predominant vortex shedding pattern will change from the normal vortex shedding mode to the oblique vortex shedding mode. At $Re = 100$, the vortex tube behind the vertical extension is perpendicular to the incoming flow, the axis flow velocity is close to zero. Due to the oblique vortex shedding phenomenon, the fluctuations of the axis flow velocities along the vertical section increase with Reynolds number. At the curved section, the axial flow velocity increases with the inclined angle ϕ and approaches to the maximum value at the junction of the curved and horizontal sections of two cylinders for each spacing ratio except for the cases of $L/D = 1.25$ and 1.5 . The axial velocity of the curved section for each cylinder at $Re = 300$ and 500 is much larger than that at $Re = 100$, where the existence of the high streamwise vorticity strength causes the increase of the axial velocity. At $Re = 300$ and 500 , the axial flow velocity is remained to be

zero at $L/D = 1.25$ and 1.5 along the curved spans of two cylinders. At the horizontal extensions of two curved cylinders, the axial flow velocity reaches a maximum of 67% of the free-stream velocity at small spacing ratio $L/D = 1.25$. It is interesting to note that at low Reynolds number $Re = 100$, the axial flow velocity is almost zero at $L/D = 1.5$. As Re increases to 300 and 500 , the axial flow velocity increases with L/D and reaches to a maximum of 88% of the free-stream velocity at $L/D = 5$. Along the horizontal extensions of two cylinders, the axial flow velocity decreases to about 10% and 7% of the free-stream velocity for each cylinder at $L/D = 1.25$, respectively.

4.4. Mean pressure coefficients

The variations of the mean pressure coefficients on the surfaces of two side-by-side curved cylinders at different horizontal planes $z/D = 27.5, 17.5$ and 12 for $Re = 300$ are presented in Fig. 18. In general, the distributions of the mean pressure coefficient \bar{C}_p for both two curved cylinders are almost symmetrical about $\theta = 180^\circ$ (i.e. the base point on the cylinder surfaces) at different z/D , similar to those for flow past straight cylinders (Lam et al., 2008). However, it is interesting to note that the distributions of mean pressure coefficients for C1 and C2 at $z/D = 12$ are significantly different from those at $z/D = 17.5$ and 27.5 , where the fluctuation amplitude of \bar{C}_p is significantly reduced from 1.0 to 0.5 along the span, the vortex shedding is suppressed at $z/D = 12$ for the curved ellipse cross section. The inclination angle of the curved cylinder increases when close to the horizontal extension, leading to the decreasing of normal velocity component. Similar variation trend of the pressure coefficient with spanwise depth is observed for a single curved cylinder (Gallardo et al., 2014a,b). With the increase of the inclination angle, the surface pressure coefficient decreases. The separation points are found to be more sensitive to the variation of the spacing ratios. The positions of separation points are located about $\theta = 80^\circ$ for $3 \leq L/D \leq 5$ at

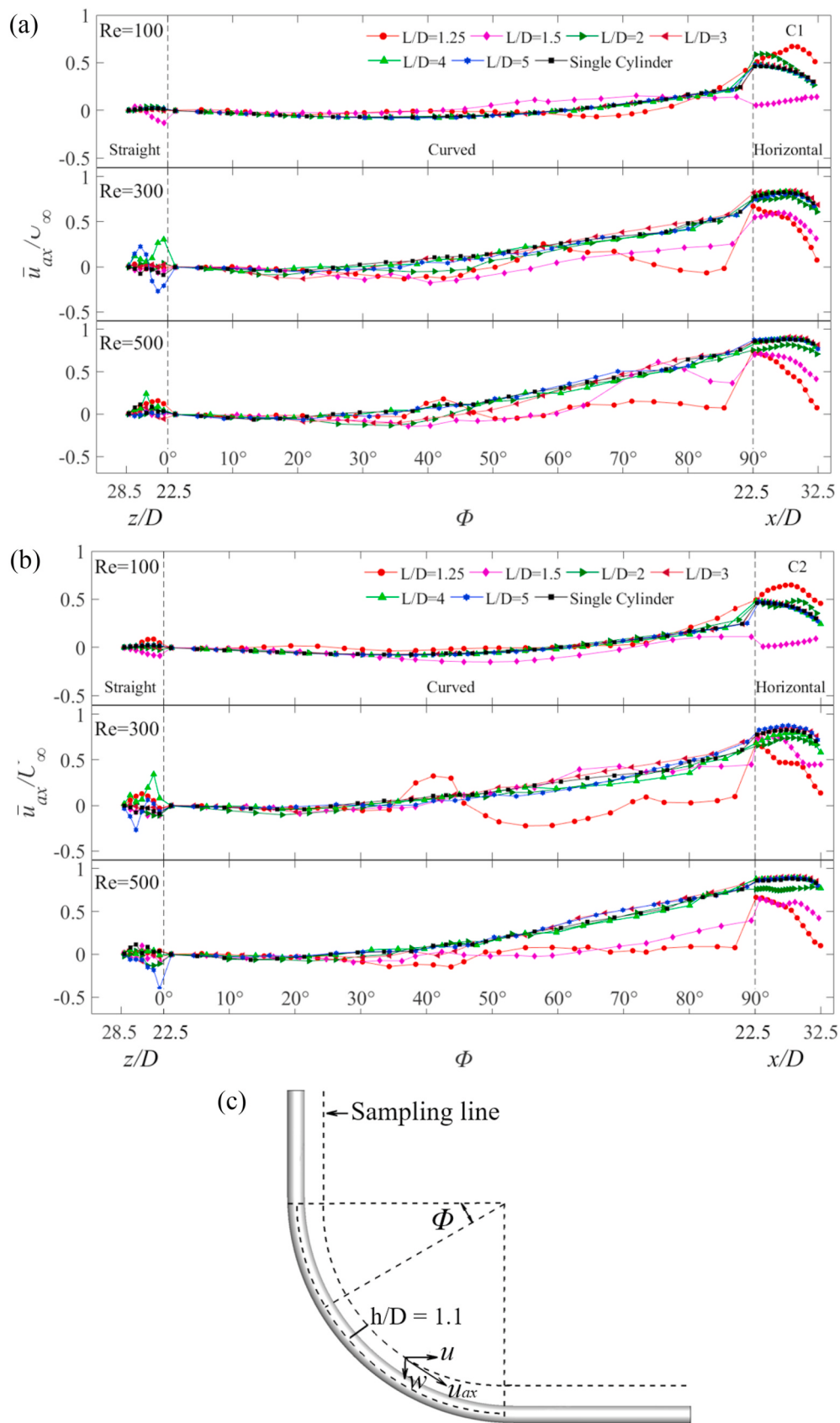


Fig. 17. Comparison of the axial velocity along the spans of two curved cylinders at different spacing ratios for $Re = 100, 300$ and 500 : (a) C1, (b) C2, (c) definition of the axial velocity.

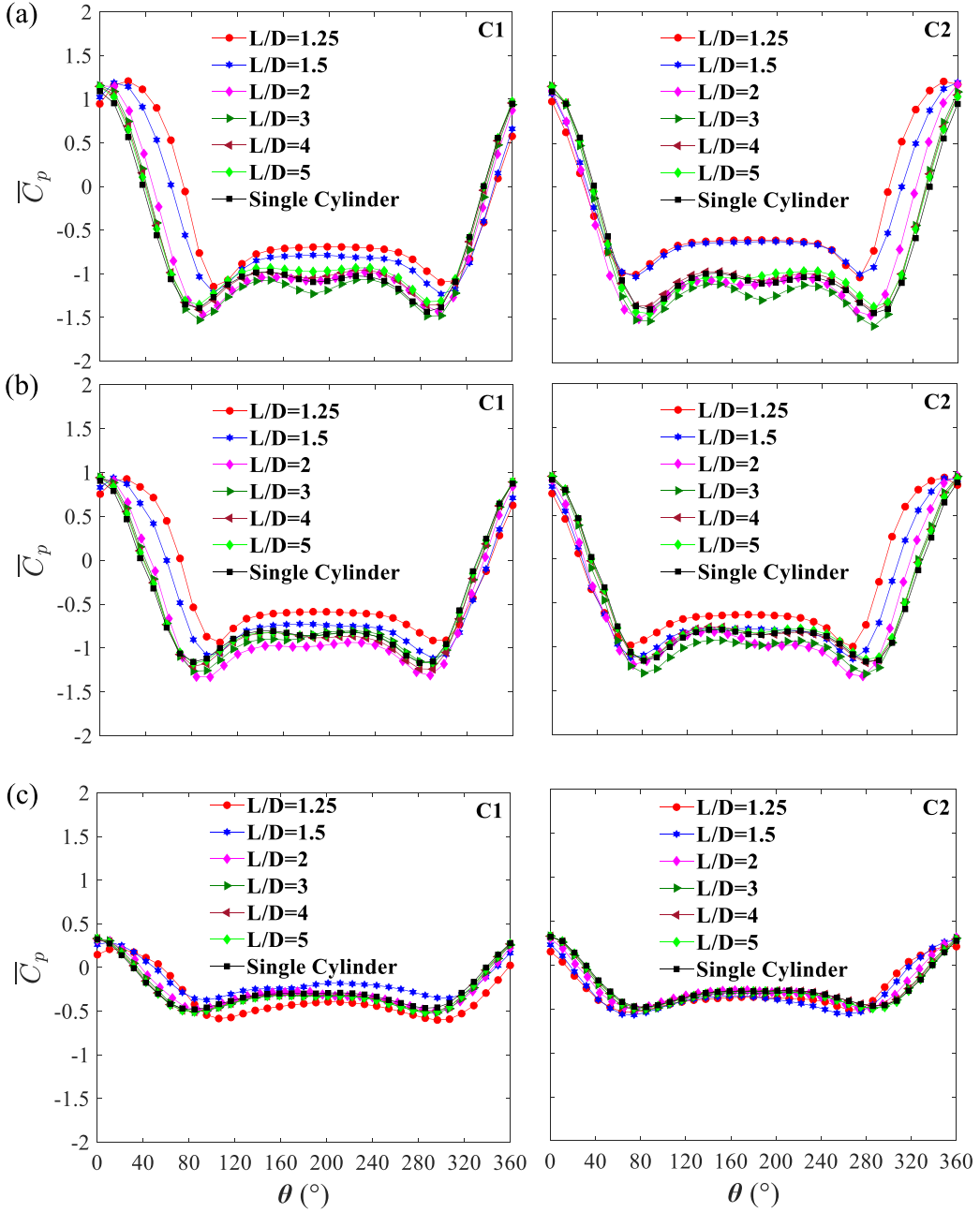


Fig. 18. Pressure coefficient distributions around two curved cylinders for $Re = 300$ at different spanwise locations: (a) $z/D = 27.5$, (b) $z/D = 17.5$, (c) $z/D = 12$.

different Reynolds numbers, similar to that of a single cylinder. However, the separation point for C2 is located at $\theta = 100^\circ$ for $L/D = 1.25$ and 1.5.

Fig. 19 depicts the variations of the base pressure coefficient \bar{C}_{pb} and stagnation pressure coefficient \bar{C}_{ps} along the stagnation lines from the vertical extension to the junction of curved segment and horizontal extension at different spacing ratios for $Re = 100, 300$ and 500, respectively. The base pressure coefficient \bar{C}_{pb} and stagnation pressure coefficient \bar{C}_{ps} are defined as the pressure coefficient at the base line and the front stagnation line (Tong et al., 2015). The fluctuation of pressure causes the emergence of spanwise flow, resulting into the oblique vortex shedding (Hammache and Gharib, 1991). The stagnation pressure coefficient does not vary with z/D at the same spacing ratio in the vertical extension, indicating that the upstream flow conditions are irresponsible to the oblique vortex shedding in the wake. Due to the spanwise velocity

reduce along the span, the absolute values of \bar{C}_{pb} and \bar{C}_{ps} decrease monotonically with increasing of s/D , and approach to zero at the junction of the curved segment and the horizontal extension, in consistent with those of a single curved cylinder observed by Miliou et al. (2007) and Canabes (2010). The base pressure coefficient is sensitive to the variation of flow instability and Reynolds number, since the change of base pressure coefficient becomes more irregular with the increase of Reynolds number, in agreement with the results for a straight cylinder obtained by Williamson (1996). The values of stagnation of pressure coefficients increase with L/D for each curved cylinder. However, the absolute value of base pressure at $L/D = 4$ is larger than that of a single cylinder.

4.5. Strouhal number

The non-dimensional vortex shedding frequency Strouhal

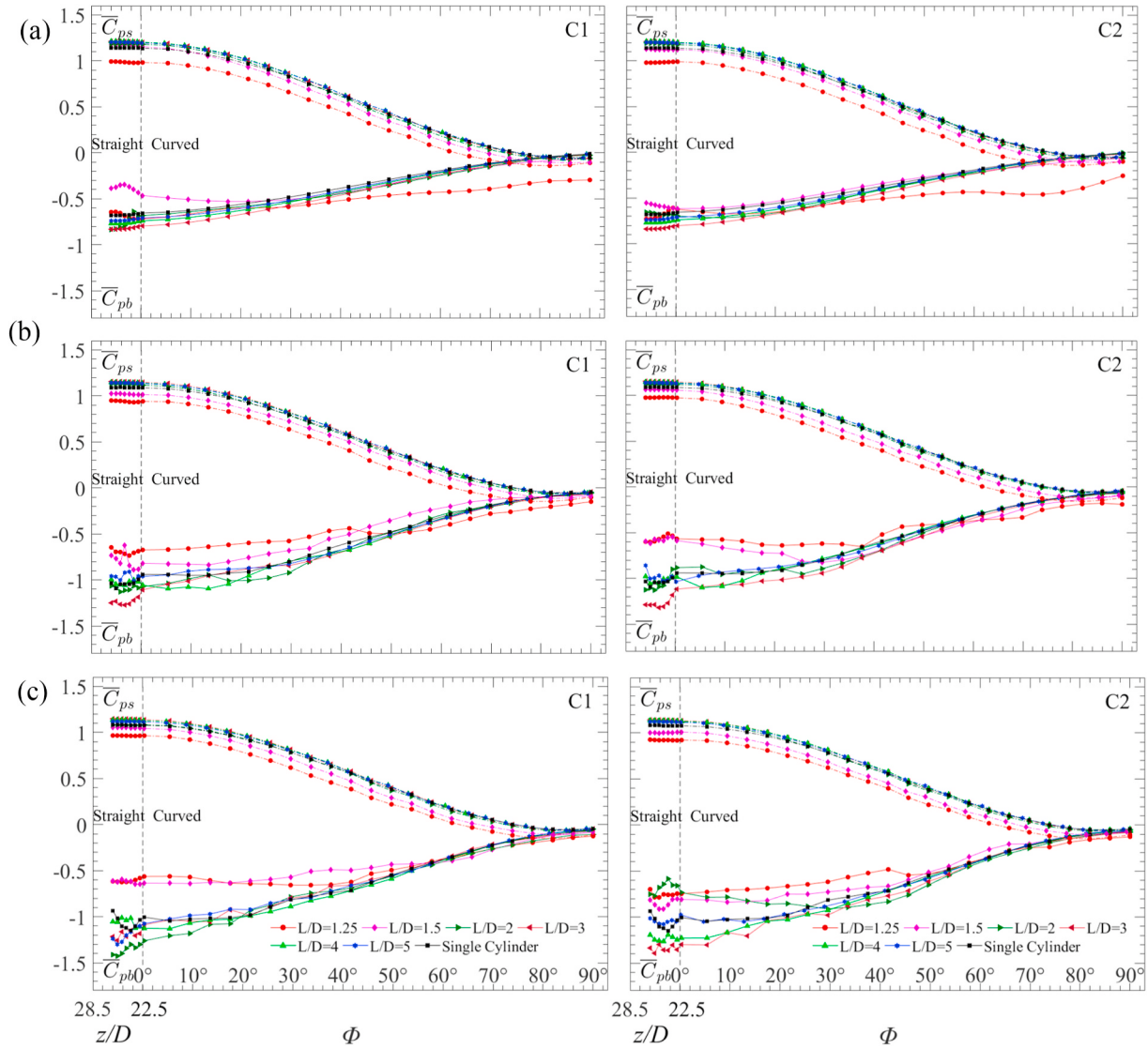


Fig. 19. Mean pressure coefficient distributions along the span of the curved cylinder at different spacing ratios: (a) $Re = 100$, (b) $Re = 300$, (c) $Re = 500$.

number $St = f_s D/U$, is obtained by Fast Fourier Transform (FFT) analysis of the transverse flow velocity, which is extracted from a distance of $5D$ behind the axis of curved cylinder at different spanwise locations. Fig. 20 shows the power spectra of the transverse flow velocity at different spacing ratios for $Re = 300$. At small spacing ratios $1.25 \leq L/D \leq 2$, multiple harmonic peaks are observed in the power spectra for two cylinders. With increasing of L/D , two prominent peaks are observed at different spanwise locations and the spectral amplitude decreases along the spanwise of the curved cylinders, which is similar with the literature results of flow past the inclined cylinder and curved cylinder (Zhao et al., 2009; Gallardo et al., 2014a,b). Fig. 21 shows the variation of the Strouhal number with spacing ratio for both two side-by-side curved cylinders, which is determined based on the vortex shedding frequency corresponding to the primary peak. The Strouhal number for each cylinder increases with L/D and approaches to that of a single cylinder at large spacing ratios $L/D = 4$ and 5. In general, the Strouhal number at the vertical extension $z/D = 27.5$ is significantly larger than that at $z/D = 12$. At $L/D = 3$, the discrepancies of the Strouhal numbers along the span decrease. The interaction between two cylinders is reduced at large spacing ratios $L/D = 4$ and 5, the Strouhal number is almost identical to that of a single curved cylinder.

5. Conclusions

A series of three-dimensional numerical simulations are performed to investigate flow past two side-by-side curved cylinders. The effects of the Reynolds number and spacing ratio on the wake topologies, time-average flow fields and mean pressure coefficient distributions are studied. The results are summarized as follows.

- (1) The wake behind the vertical straight sections of the two side-by-side cylinders are classified into four flow regimes: a single bluff body pattern, biased flow pattern, coupling vortex shedding pattern and co-shedding pattern. As Re increases, the critical spacing ratio for different flow regimes decreases. The flows along the curved sections of two cylinders are classified into five flow regimes: normal vortex shedding, vortex dislocation, oblique vortex shedding, non-shedding and shear layer instability regimes.
- (2) The reverse flow is found to be significantly suppressed at the spanwise location close to the horizontal extension due to the effect of axial flow velocity. With the increase of L/D , the axial flow velocity increases and the streamline pattern behind two cylinders behaves from the asymmetrical to symmetrical distribution.

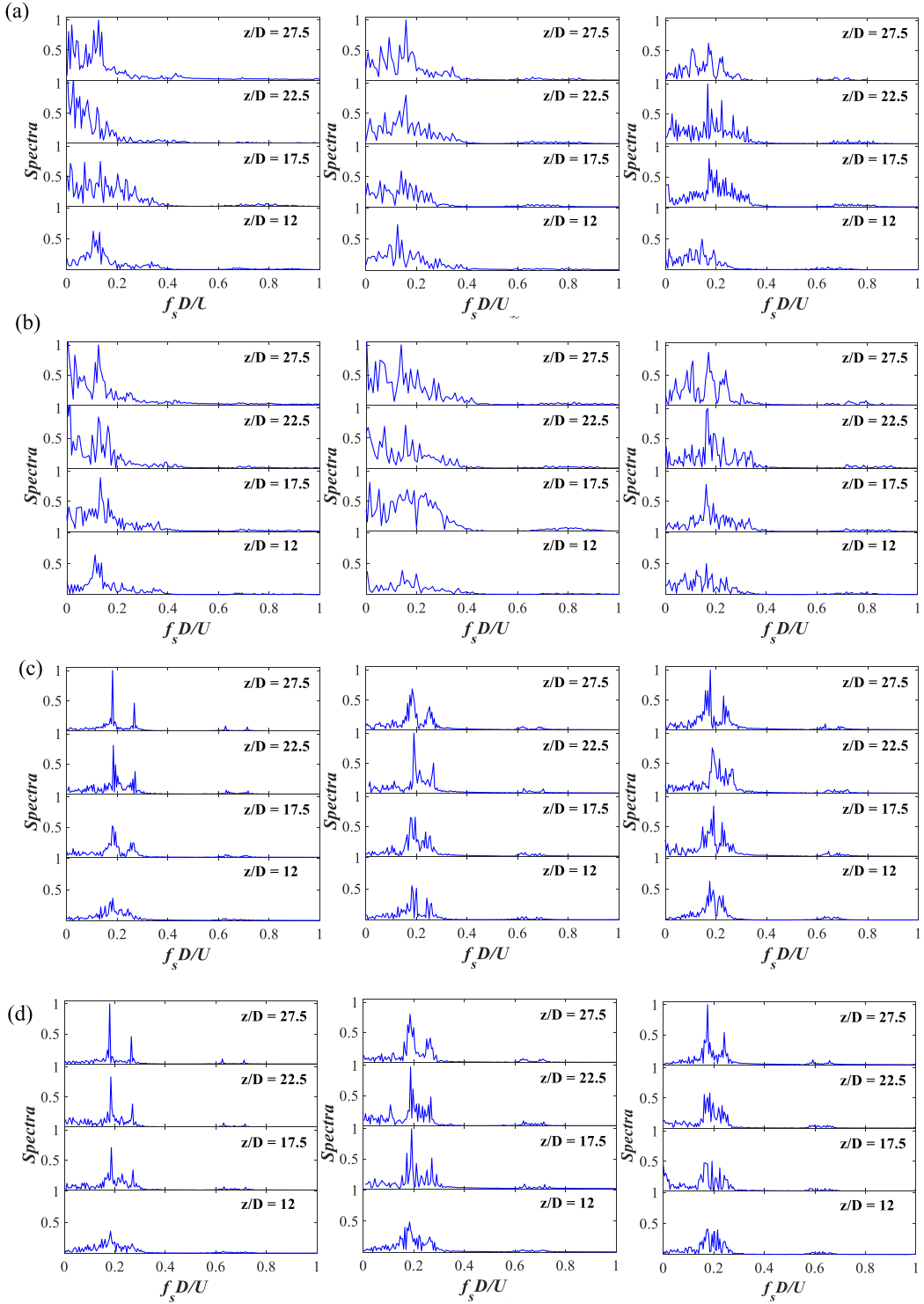


Fig. 20. Power spectra of the transverse flow velocity for two curved cylinders at different L/D for $Re = 300$. (a) C1, $L/D = 1.25, 1.5$ and 2 (from left to right), (b) C2, $L/D = 1.25, 1.5$ and 2 (from left to right), (c) C1, $L/D = 3, 4$ and 5 (from left to right), (d) C2, $L/D = 3, 4$ and 5 (from left to right).

(3) The Reynolds stress, the vortex strengths and the mean pressure coefficients behind two curved cylinders are significantly reduced along the curved section. The absolute value of base pressure coefficient decreases with the increase of L/D . As the Reynolds number increases, the base coefficients of two curved cylinders increase.

Data availability

The data that support the finding of this study are available from the corresponding author upon reasonable request.

CRediT authorship contribution statement

Yangyang Gao: Conceptualization, Numerical simulation,

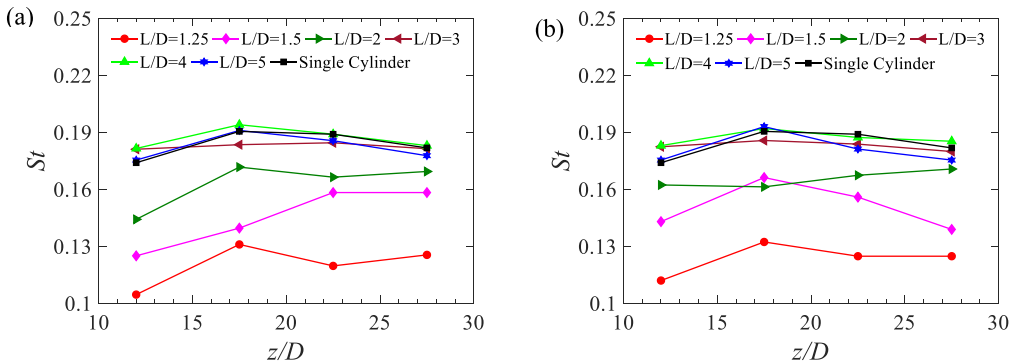


Fig. 21. Variation of Strouhal numbers with z/D at different spacing ratios for $Re = 300$: (a) C1, (b) C2.

Supervision, Investigation, Writing – review & editing. **Jianyong He:** Numerical model, Data curation, Investigation, Writing – original draft. **Muk Chen Ong:** Writing – review & editing. **Ming Zhao:** Writing – review & editing. **Lizhong Wang:** Writing – review & editing.

Declaration of competing interest

The authors declare that they have no known competing financial interests or personal relationships that could have appeared to influence the work reported in this paper.

Acknowledgements

This research was supported by National Nature Science Foundation of China (Grant No. 51939010), Major Science and Technology Project of Sanya (No. SKJC-KJ-2019KY03), Joint Fund of Zhejiang Provincial Natural Science Foundation (Grant No. LHZ19E090004).

References

- Afghan, I., Kahil, Y., Benhamadouche, S., Sagaut, P., 2011. Large eddy simulation of the flow around single and two side-by-side cylinders at subcritical Reynolds numbers. *Phys. Fluids* 23 (7), 075101.
- Alam, M.M., Zhou, Y., 2007. Flow around two side-by-side closely spaced circular cylinders. *J. Fluid Struct.* 23, 799–805.
- Alam, M.M., Zhou, Y., 2013. Intrinsic features of flow around two side-by-side square cylinders. *Phys. Fluids* 25 (8), 085106.
- Alam, M.M., Moriya, M., Sakamoto, H., 2003. Aerodynamic characteristics of two side-by-side circular cylinders and application of wavelet analysis on the switching phenomenon. *J. Fluid Struct.* 18, 325–346.
- Alam, M.M., Zhou, Y., Wang, X.W., 2011. The wake of two side-by-side square cylinders. *J. Fluid Mech.* 669, 432–471.
- Assi, G.R.S., Srinil, N., Freire, C.M., Korkischko, I., 2014. Experimental investigation of the flow-induced vibration of a curved cylinder in convex and concave configurations. *J. Fluid Struct.* 44, 52–66.
- Barkley, D., Henderson, R.D., 1996. Three-dimensional floquet stability analysis of the wake of a circular cylinder. *J. Fluid Mech.* 322, 215–241.
- Batcho, P., Karniadakis, G.E., 1991. Chaotic transport in two- and three-dimensional flow past a cylinder. *Phys. Fluids A3*, 1051–1062.
- Batham, J.P., 1973. Pressure distributions on circular cylinders at critical Reynolds numbers. *J. Fluid Mech.* 57 (2), 209–228.
- Bearman, P.W., Wadcock, A.J., 1973. The interaction between a pair of circular cylinders normal to a stream. *J. Fluid Mech.* 61, 499–511.
- Braza, M., Chassaing, P., Minh, H.H., 1986. Numerical study and physical analysis of the pressure and velocity fields in the near wake of a circular cylinder. *J. Fluid Mech.* 165, 79–130.
- Burbeau, A., Sagaut, P., 2002. Simulation of a viscous compressible flow past a circular cylinder with high-order discontinuous Galerkin methods. *Comput. Fluids* 31, 867–889.
- Canabes, P.G., 2010. Direct numerical simulation of the flow past a curved circular cylinder. Master thesis. Norwegian University of Science and Technology.
- Clift, R., Grace, J.R., Weber, M.E., 1978. Bubbles, Drops, and Particles. Academic, New York.
- Dong, S., Karniadakis, G.E., Ekmekci, A., Rockwell, D., 2006. A combined direct numerical simulation–particle image velocimetry study of the turbulent near wake. *J. Fluid Mech.* 569, 185–207.
- Gallardo, J.P., Pettersen, B., Andersson, H.I., 2013. Effects of free-slip boundary conditions on the flow around a curved circular cylinder. *Comput. Fluids* 86, 389–394.
- Gallardo, J.P., Andersson, H.I., Pettersen, B., 2014a. Turbulent wake behind a curved circular cylinder. *J. Fluid Mech.* 742, 192–229.
- Gallardo, J.P., Andersson, H.I., Pettersen, B., 2014b. Coherence and Reynolds stresses in the turbulent wake behind a curved circular cylinder. *J. Turbul.* 15, 883–904.
- Gao, Y., Liu, C., Zhao, M., Wang, L., Zhu, R., 2020. Experimental investigation on flow past two and three side-by-side inclined cylinders. *J. Fluid Eng.* 142, 11201–1.
- Hammache, M., Gharib, M., 1991. Experimental study of the parallel and oblique vortex shedding from circular cylinders. *J. Fluid Mech.* 232, 567–590.
- Homann, F., 1936. Influence of higher viscosity on flow around cylinder. *Fortsch. Gebiete Ingenieurw.* 17, 1–10.
- Ishigai, S., Nishikawa, E., Nishimura, K., Cho, K., 1972. Experimental study on structure of gas flow in tube banks with tube axes normal to flow: Part 1, Karman vortex flow around two tubes at various spacings. *Bull. JSME* 15, 949–956.
- Jiang, F., Pettersen, B., Andersson, H.I., 2018a. Influences of upstream extensions on flow around a curved cylinder. *Eur. J. Mech. B Fluid* 67, 79–86.
- Jiang, F., Pettersen, B., Andersson, H.I., Kim, J., Kim, S., 2018b. Wake behind a concave curved cylinder. *Phys. Rev. Fluids* 3, 049804.
- Jiang, F., Pettersen, B., Andersson, H.I., 2019. Turbulent wake behind a concave curved cylinder. *J. Fluid Mech.* 878, 663–699.
- Kang, S., 2003. Characteristics of flow over two circular cylinders in a side-by-side arrangement at low Reynolds numbers. *Phys. Fluids* 15, 2486–2498.
- Kang, S., Choi, H., Lee, S., 1999. Laminar flow past a rotating circular cylinder. *Phys. Fluids* 11, 3312–3321.
- Kravchenko, A.G., Moin, P., 2000. Numerical studies of flow over a circular cylinder at $Re_D = 3900$. *Phys. Fluids* 12 (2), 403–417.
- Lam, K., Gong, W.Q., So, R.M.C., 2008. Numerical simulation of cross-flow around four cylinders in an in-line square configuration. *J. Fluid Struct.* 24, 34–57.
- Lee, S., Paik, K., Srinil, N., 2020. Wake dynamics of a 3D curved cylinder in oblique flows. *Ocean Eng.* 12, 501–517.
- Lei, C., Cheng, L., Kavanagh, K., 2001. Spanwise length effects on three-dimensional modelling of flow over a circular cylinder. *Comput. Methods Appl. Mech. Eng.* 190, 2909–2923.
- Meneghini, J.R., Saltara, F., Siqueira, C.L.R., Ferrari, J.J.A., 2001. Numerical simulation of flow interference between two circular cylinders in tandem and side-by-side arrangements. *J. Fluid Struct.* 15 (2), 327–350.
- Miliou, A., Sherwin, S.J., Graham, J.M.R., 2003. Wake topology of curved cylinders at low Reynolds numbers. *Flow, Turbul. Combust.* 71, 147–160.
- Miliou, A., De Vecchi, A., Sherwin, S., Graham, J., 2007. Wake dynamics of external flow past a curved circular cylinder with the free stream aligned with the plane of curvature. *J. Fluid Mech.* 592, 89–115.
- Mittal, R., Balachandar, S., 1995. Effect of three-dimensionality on the lift and drag of nominally two-dimensional cylinders. *Phys. Fluids* 7, 1841–1865.
- Muddada, S., Patnaik, B.S.V., 2010. An active flow control strategy for the suppression of vortex structures behind a circular cylinder. *Eur. J. Mech. B Fluid* 29, 93–104.
- Norberg, C., 1994. An experimental investigation of the flow around a circular cylinder: influence of aspect ratio. *J. Fluid Mech.* 258 (1), 287–316.
- Norberg, C., 2003. Fluctuating lift on a circular cylinder: review and new measurements. *J. Fluid Struct.* 17 (1), 57–96.
- Rajani, B., Kandasamy, A., Majumdar, S., 2009. Numerical simulation of laminar flow past a circular cylinder. *Appl. Math. Model.* 33 (3), 1228–1247.
- Schlichting, H., Gersten, G., 2003. Boundary Layer Theory. Springer, Berlin.
- Shang, J.K., Stone, H.A., Smits, A.J., 2018. Flow past a finite cylinder of constant curvature. *J. Fluid Mech.* 837, 896–915.
- Sharman, B., Lien, F.S., Davidson, L., Norberg, C., 2005. Numerical predictions of low Reynolds number flows over two tandem circular cylinders. *Int. J. Numer. Methods Fluid.* 47, 423–447.
- Stansby, P.K., Slaouti, A., 1993. Simulation of vortex shedding including blockage by the random-vortex and other methods. *Int. J. Numer. Methods Fluid.* 17, 1003–1013.
- Sumner, D., 2010. Two circular cylinders in cross-flow: a review. *J. Fluid Struct.* 26, 849–899.

- Sumner, D., Wong, S.S.T., Price, S.J., Païdoussis, M.P., 1999. Fluid behaviour of side-by-side circular cylinders in steady cross-flow. *J. Fluid Struct.* 13, 309–338.
- Thapa, J., Zhao, M., Cheng, L., Zhou, T., 2015. Three-dimensional simulations of flow past two circular cylinders in side-by-side arrangements at right and oblique attacks. *J. Fluid Struct.* 55, 64–83.
- Thom, A., 1933. The flow past circular cylinder at low speeds. *Proc. Royal Soc. A* 141, 651–669.
- Tong, F., Cheng, L., Zhao, M., Zhou, T., Chen, X.B., 2014. The vortex shedding around four circular cylinders in an in-line square configuration. *Phys. Fluids* 26, 1–20.
- Tong, F., Cheng, L., Zhao, M., 2015. Numerical simulations of steady flow past two cylinders in staggered arrangements. *J. Fluid Mech.* 765, 114–149.
- Vu, H.C., Ahn, J., Hwang, J.H., 2016. Numerical simulation of flow past two circular cylinders in tandem and side-by-side arrangement at low Reynolds numbers. *KSCE J. Civ. Eng.* 20, 1594–1604.
- Wang, Z.J., Zhou, Y., 2005. Vortex interactions in a two side-by-side cylinder near-wake. *Int. J. Heat Fluid Flow* 26, 362–377.
- Williamson, C.H.K., 1988. The existence of two stages in the transition to three dimensionality of a cylinder wake. *Phys. Fluids* 31, 3165–3168.
- Williamson, C.H.K., 1989. Oblique and parallel modes of vortex shedding in the wake of a circular cylinder at low Reynolds numbers. *J. Fluid Mech.* 206 (3), 579–627.
- Williamson, C., 1996. Vortex dynamics in the cylinder wake. *Annu. Rev. Fluid Mech.* 28, 477–539.
- Xu, S.J., Zhou, Y., So, R.M.C., 2013. Reynolds number effects on the flow structure behind two side-by-side cylinders. *Phys. Fluids* 15, 1214–1219.
- Zhao, M., Cheng, L., Zhou, T., 2009. Direct numerical simulation of three-dimensional flow past a yawed circular cylinder of infinite length. *J. Fluid Struct.* 25 (5), 831–847.
- Zhao, M., Thapa, J., Cheng, L., Zhou, T., 2013. Three-dimensional transition of vortex-shedding flow around a circular cylinder at right and oblique attacks. *Phys. Fluids* 25, 014105.
- Zhu, H., Zhou, D., Bao, Y., Wang, R., Lu, J., Fan, D., Han, Z., 2018. Wake characteristics of stationary catenary risers with different incoming flow directions. *Ocean. Eng.* 167, 142–155.
- Zhu, H., Wang, R., Bao, Y., Zhou, D., Ping, H., Han, Z., Sherwin, S.J., 2019. Flow over a symmetrically curved circular cylinder with the free stream parallel to the plane of curvature at low Reynolds number. *J. Fluid Struct.* 87, 23–38.